STRUCTURAL, ELECTRONIC AND MAGNETIC PROPERTIES OF GROUP III MONOCHALCOGENIDE NANORIBBONS

A THESIS SUBMITTED TO
THE GRADUATE SCHOOL OF ENGINEERING AND SCIENCE
OF BILKENT UNIVERSITY
IN PARTIAL FULFILLMENT OF THE REQUIREMENTS FOR
THE DEGREE OF
MASTER OF SCIENCE
IN
MATERIAL SCIENCE AND NANOTECHNOLOGY

By
Emin Aliyev
May 2025

Structural, Electronic and Magnetic Properties of Group III Monochalcogenide Nanoribbons
By Emin Aliyev
May 2025

We certify that we have read this thesis and that in our opinion it is fully adequate, in scope and in quality, as a thesis for the degree of Master of Science.

Seymur Jahangirov(Advisor)

Hâldun Sevinçli

Aybey Moğulkoç

Approved for the Graduate School of Engineering and Science:

Orhan Arıkan
Director of the Graduate School

ABSTRACT

STRUCTURAL, ELECTRONIC AND MAGNETIC PROPERTIES OF GROUP III MONOCHALCOGENIDE NANORIBBONS

Emin Aliyev
M.S. in Material Science and Nanotechnology
Advisor: Seymur Jahangirov
May 2025

Owing to the promising optoelectronic and thermoelectric properties of two-dimensional (2D) group III–VI materials (MXs), their nanoribbons (NRs) have attracted notable attention as an emerging class of quasi-one-dimensional (quasi-1D) nanostructures. Due to the fact that the most stable 2D monolayer polymorph of MXs is the 1H phase, to date, existing studies in the literature have predominantly focused on the NRs formed from 1H phase MXs. Nevertheless, NRs of the 1T phase have received little to no attention. Employing *ab initio* simulations based on density functional theory, we systematically compared the thermodynamic stability of hydrogen-passivated and unpassivated 1T and 1H zigzag (ZNR) and armchair (ANR) edge NRs of GaS, GaSe, and InSe. Our results reveal that nonpolar 1T phase MX ZNRs are thermodynamically more favorable than polar 1H MX ZNRs at widths up to 34 nm, a range that is realizable through contemporary experimental fabrication techniques. On the other hand, as both 1H and 1T ANRs are nonpolar, 1T is more favorable only in unpassivated cases in very narrow widths of up to 3.3nm in the case of InSe ANRs. Furthermore, unlike metallic 1H ZNRs, 1T ZNRs remain semiconductors and retain Mexican-hat-shaped (MHS) top valence bands. Complementarily, hydrogenation energies of 1T InSe NRs are positive, and due to the edge-localized states, the 1T unpassivated ZNRs possess nearly flat top valence bands. These electronic properties present compelling opportunities for exploiting 1T MX NRs in spintronic applications. We demonstrate that, upon hole doping, these MX NRs develop itinerant magnetization across a broad range of carrier densities and display half-metallic behavior, with only one spin channel intersecting the Fermi level. Moreover, the spin-polarization energies (SPE) of these NRs increase remarkably relative to their 2D counterparts, indicating stronger stability of the ferromagnetic state. We elucidate that the SPE of NRs strongly depends on the

degree of edge-localization of the carriers along the width of NRs, which in turn depends on the edge passivation, width, and edge shape of NRs. Overall, this study highlights the critical interplay between the thermodynamic favorability of the novel 1T phase MX NRs below certain critical widths and the resulting electronic and magnetic properties, which together enable their promising applications in spintronics and nanoelectronics.

Keywords: Density functional theory, nanoribbons, monochalcogenides, half-metallicity, hole-doping, ferromagnetism.

ÖZET

GRUP III MONOKALKOJENÜR NANOŞERİTLERİN YAPISAL, ELEKTRONİK VE MANYETİK ÖZELLİKLERİ

Emin Aliyev
Malzeme Bilimi ve Nanoteknoloji, Yüksek Lisans
Tez Danışmanı: Seymur Jahangirov
Mayıs 2025

İki boyutlu (2B) grup III–VI malzemeler (MX'ler) olağanüstü optoelektronik ve termoelektrik özellikler göstermektedirler, bu nedenle bu malzemelerin nanoşeritleri (NŞ'ler) son yıllarda kuasi tek boyutlu (kuasi-1B) nanoyapılar olarak yoğun ilgi görmüştür. En kararlı 2B monolayer polimorfın 1H fazı olması sebebiyle, literatürdeki çalışmalar ağırlıklı olarak 1H fazlı MX NŞ'lerine odaklanmıştır; ancak 1T fazlı NŞ'ler neredeyse hiç incelenmemiştir. Bu eksikliği gidermek amacıyla, yoğunluk fonksiyonel teorisine dayalı ab initio simülasyonlar ile hidrojen pasivasyonlu ve pasivasyonsuz 1T ile 1H fazlı GaS, GaSe ve InSe zigzag (ZNŞ) ve koltuk (KNŞ) kenarlı NŞ'lerinin termodinamik kararlılıkları sistematik olarak karşılaştırılmıştır. Elde edilen sonuçlar, 34 nm'e kadar olan genişliklerde, çağdaş deneysel üretim teknikleriyle gerçekleştirilmesi mümkün bir aralıkta, apolar 1T fazlı MX ZNŞ'lerinin, polar 1H fazlı MX ZNŞ'lerine kıyasla termodinamik olarak daha kararlı olduğunu göstermektedir. Buna karşılık, hem 1H hem de 1T fazlı ANR'ler apolar olduğundan, 1T sadece pasivasyonsuz durumlarda, InSe ANR'lerde en fazla 3,3 nm'ye kadar olan çok dar genişliklerde daha kararlıdır. Ayrıca, metalik davranış sergileyen 1H ZNŞ'lerin aksine, 1T fazlı ZNŞ'ler yarıiletken karakterini koruyarak üst valans bandında Meksika şapkası biçimli (MSB) bant yapısını muhafaza etmektedir. Buna ek olarak, 1T InSe NŞ'lerin hidrojenasyon enerjileri pozitif olup, kenar-yerelleşmiş durumlar nedeniyle pasivasyonsuz 1T ZNŞ'ler neredeyse düz üst valans bantlarına sahiptir. Söz konusu elektronik özellikler, 1T fazlı MX NŞ'lerinin spintronik uygulamalarda kullanımı için önemli fırsatlar sunmaktadır. Çalışmamızda, deşik katkılanması sonucunda bu MX NŞ'lerinin geniş bir taşıyıcı yoğunluğu aralığında gezici manyetizasyon geliştirdiğini ve yalnızca bir spin kanalının Fermi seviyesini kestiği yarı-metal davranışı sergilediğini gösteriyoruz. Ayrıca, söz konusu NŞ'lerin

spin polarizasyon enerjileri (SPE), 2B karşıtlarına kıyasla önemli ölçüde arttığını ve ferromanyetik durumun daha güçlü bir şekilde kararlı hale geldiğini ortaya koymaktayız. NŞ'lerde SPE'nin, taşıyıcıların genişlik boyunca kenarlarda lokalize olma derecesine güçlü şekilde bağımlı olduğunu ve bunun da kenar pasifleştirmesi, genişlik ve kenar şekli gibi faktörlere bağlı olduğunu açıklıyoruz. Genel olarak, bu çalışma, belirli kritik genişliklerin altında yeni 1T MX NŞ'lerin termodinamik kararlılığı ile elektronik ve manyetik özellikleri arasındaki kritik etkileşimi vurgulayarak, söz konusu yapıların spintronik ve nanoelektronik uygulamalardaki potansiyelini ortaya koymaktadır.

Anahtar sözcükler: Yoğunluk fonksiyonel teorisi, nanoşeritler, monokalkojenitler, yarı-metallik, deşik katkılama, ferromanyetizma.

Acknowledgement

I am deeply grateful to my supervisor, Assoc. Prof. Seymur Jahangirov, for his continuous support and guidance throughout my master's studies. I cherish the time we shared diving into academic questions or exploring completely different topics.

I sincerely thank Dr. Arash Mobaraki for his guidance on DFT calculations, academic mentorship, and friendship. This work would not be possible without the numerous hours we spent working through research questions and seeking solutions together.

I would like to thank my defense committee members, Prof. Dr. Hâldun Sevinçli and Prof. Dr. Aybey Moğulkoç, for their time to thoroughly review my thesis and offer helpful suggestions. I am particularly grateful to Prof. Dr. Hâldun Sevinçli, whose thoughtful guidance during our discussions played a crucial role in shaping many aspects of this work.

I am also grateful to Asst. Prof. Fahri Alkan for introducing me to the world of quantum mechanics and computational material science, which sparked my interest and formed the trajectory leading to this thesis.

My heartfelt thanks go to the friends I've been fortunate to meet these last two years for their help, encouragement, and the countless moments we shared that brightened even the most challenging days.

Finally, I am immensely grateful to my mother, father, brother, and good old friends for always being there for me.

I acknowledge support from the TÜBİTAK-ANAS project No. 120N296 and TÜBİTAK project No. 124F108. The calculations were performed at TÜBİTAK ULAKBİM, High Performance and Grid Computing Center (TRUBA resources) and National Center for High-Performance Computing of Turkey (UHeM) under grant number 1007742020.

Contents

List of Figures

List of Tables

Chapter 1

Introduction

Since the isolation of two-dimensional (2D) graphene monolayer from graphite [4] and the fabrication of further confined 1D materials such as graphene nanotubes [5] and nanoribbons (NRs) [6], the exploration of low-dimensional structures has attracted considerable attention from researchers. It became evident that dimensional confinement in 2D leads to the emergence of a wide range of novel electronic, magnetic, and optical properties that were absent in the bulk counterpart. Moreover, NRs fabricated by confining 2D layers laterally [7, 8], further broadened the spectrum of properties, and enabled fine-tuning of these properties by altering the width [9], edge shapes, and various edge functionalizations of ribbons [10, 11]. Size and tunable properties made NRs attractive candidates for nanoscale applications in a wide range of fields, including spintronics [12], optoelectronics [13, 14], catalysis [15], and biomedical applications [16].

Honeycomb-like shape of graphene monolayer enable fabrication of its nanoribbons (GNRs) with two primary distinct edge shapes: armchair (AGNR) and zigzag (ZGNR). AGNRs depending on the width, can exhibit either metallic or semiconducting behavior [17]. Consequently, various field effect transistors were successfully fabricated from a few atom-wide AGNRs [18, 19, 20]. On the other hand, all ideal ZGNRs are metallic and possess localized edge states, independent of the ZGNR's width. Nevertheless, theoretical and experimental studies have

shown that one can passivate the dangling bonds at edges by hydrogenation, oxidation, or functionalization with other compounds and open up the band gap in ZGNR's [21].

While GNRs have been extensively investigated, the emergence of diverse two-dimensional materials has broadened the exploration of NR structures beyond carbon systems [22]. Among these, group III metal monochalcogenides (MXs, M = Ga, In and X = S, Se) have garnered substantial research interest in the past years, offering distinctive properties, due to a remarkable variety of polymorphs [23, 24, 25, 26, 27, 28, 29, 30]. To date, two phases of 2D MX compounds have been subject to extensive research: honeycomb-like trigonal prismatic (eclipsed, H) and trigonal anti-prismatic (staggered, T) phases. The ground state of GaS, GaSe, and InSe in 2D is H phase, where a unit cell consists of metal atoms sandwiched between chalcogen atoms in an X-M-M-X like arrangement. Conversely, the T phase, a metastable polymorph in the aforementioned MX systems, exhibits structural characteristics analogous to the H phase, differing principally in the crystallographic arrangement of chalcogen atoms. Specifically, within the X-M-M-X tetralayer configuration, the upper chalcogen sheet undergoes a 60° azimuthal rotation with respect to the underlying layer (see Figure 1.1) [31].

Numerous theoretical investigations [30, 32, 31] have shown that these phases of 2D MXs can be considered nearly energetically degenerate as the energy difference between them is less than k_BT at room temperature, which is possible to overcome with strain or doping. Indeed, both H and T phases 2D MXs were successfully fabricated in recent years. Few-layer and monolayer 2D structures of H-phase GaS, GaSe, and InSe were successfully synthesized with various methods [33, 34, 35, 36]. In a recent study, Jiang and co-workers demonstrated a ballistic field-effect transistor based on mechanically exfoliated 2D InSe that surpasses all previously reported silicon FETs [37]. Beyond transistor applications, H-phase MXs have been identified as highly promising for optoelectronic, spintronic, and thermoelectric devices [34, 38]. In another recent investigation, Gutierrez et al. synthesized T-phase 2D GaS films via chemical vapor deposition [24]. Likewise, T-phase GaSe monolayers have been realized through molecular beam epitaxy [23, 29]. Furthermore, 2D GaSe with T-phase–like layer formation induced

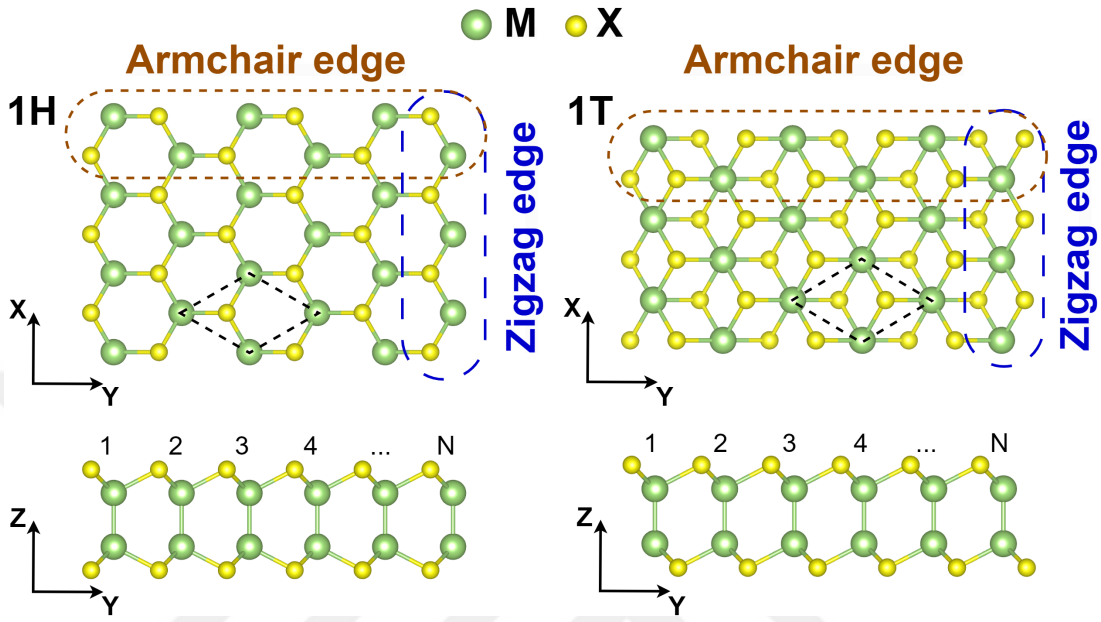

Figure 1.1: Schematic representations of 1T and 1H MX NRs and the unit cells of the corresponding 2D monolayers. Adapted from Aliyev et al. [1] under a CC BY license.

by intralayer Se atom sliding was reported to display exotic nonvolatile memory behavior characterized by a high channel current on/off ratio [25].

The distinguishing properties of 2D MXs inspired many researchers to investigate their 1D counterparts as well. To date, various 1D 1H MX nanostructures, such as nanobelts, nanowires, and NRs, have been fabricated and demonstrated to exhibit promising properties for the next generation of nanophotonics and optoelectronics [39, 40, 41, 42, 43, 44, 45, 46]. Besides, theoretical investigations of 1H MX NRs have revealed distinctive electronic and magnetic characteristics. GaS ZNRs are known to exhibit robust intrinsic ferromagnetism (FM) that persists under variable strain conditions, transitioning to antiferromagnetic (AFM) state only at significant compressive strain thresholds [47, 48]. Edge passivation also significantly modulates electronic properties: hydrogen-passivated GaS ANRs demonstrate band gap enhancement to 2.48 eV with width-independent behavior [49]. In contrast, GaS and InSe ZNRs maintain metallic character even after passivation except in ultranarrow configurations ($N \leq 4$). GaSe and InSe NRs display analogous electronic behavior to their GaS counterparts, while InSe

is also reported to exhibit promising catalytic performance in hydrogen evolution reaction [50, 51].

While the existing literature has predominantly focused on the 1H phase of MX NRs, the 1T MX NRs are left substantially underexplored. Notably, the investigation of phase transitions in nanoscale systems has attracted significant research interest owing to their profound impact on functional properties and potential applications. In various nanostructured materials, such transitions can be effectively modulated through external stimuli, including electric and magnetic fields, as well as mechanical deformation [52, 53]. Furthermore, confinement effects at narrow widths have been demonstrated to significantly influence phase stability and electronic structure [54].

In this thesis, we conducted a systematic and comprehensive study using ab initio density functional theory (DFT) calculations [55, 56] to examine how ribbon width influences the relative stability between the 1T and 1H polymorphs in both zigzag (ZNR) and armchair (ANR) edge configurations of MX nanoribbons, as well as their electronic and magnetic properties. Our results reveal that, for both hydrogen-passivated ZNRs (P-ZNRs) and unpassivated ZNRs (UP-ZNRs), the 1T-phase ZNRs remain thermodynamically preferred over their 1H-phase counterparts up to specific threshold widths of approximately 23 nm for GaS, 31 nm for GaSe, and 34 nm for InSe. This pronounced stability advantage of 1T ZNRs originates from the absence of a built-in electric field, which in the polar 1H phase leads to elevated formation energies. Moreover, the intrinsic electric field in 1H ZNRs, not only alters their atomic configuration, but also significantly impacts their electronic structure. Specifically, we demonstrate that polar 1H ZNRs exhibit metallic conductivity even after edge passivation, consistent with earlier reports [50, 49, 57, 47, 58, 48], whereas nonpolar 1T ZNRs preserve a finite band gap across all studied widths and passivation conditions.

On the other hand, we discovered that in MX armchair nanoribbons (ANRs), the intrinsic electric field polarization is absent in both 1H and 1T crystallographic phases. Consequently, the difference between formation energies of 1T and 1H phase ANRs is significantly smaller than in ZNRs, and the 1T phase demonstrates

thermodynamic favorability over the 1H phase in UP-ANRs exclusively at very narrow widths up to 3.3nm in the case of InSe. Besides, in P-ANRs, the electronic saturation of edge dangling bonds with hydrogens diminishes the edge effects and makes the 1H phase thermodynamically more favorable even at minimal NR widths.

The structural and electronic characteristics of these NRs establish the foundation for exploring their emergent magnetic properties. While the magnetic response to hole doping has been extensively investigated in the parent 2D MX systems, the effects of further spatial confinement to 1D remain largely unexplored. This dimensional reduction introduces additional quantum confinement effects and edge-state contributions that may significantly affect the charge distribution and alter the magnetic ordering mechanisms. Previous theoretical studies on MX systems have demonstrated that, upon hole doping, two-dimensional GaSe and InSe can exhibit half-metallicity and itinerant ferromagnetism within a specific range of carrier densities [3, 59]. To quantify the energetic stability of the ferromagnetic state, the spin polarization energy (SPE) is defined as the energy difference between the FM (spin-polarized) and nonmagnetic (non-spin-polarized) states, reaching up to about 3.5 meV/carrier for GaSe [3] and 10 meV/carrier for InSe [59]. Furthermore, analogous studies on GNRs have revealed GNRs with certain edge passivations also exhibit similar properties upon hole doping, and GZNRs manifest higher SPE compared to their GANR counterparts, reaching values up to 17 meV/carrier [60]. The aforementioned properties, including half-metallicity, itinerant ferromagnetism, and sizable spin polarization energies, make these materials promising candidates for spintronic applications, where control over spin-dependent transport is essential for next-generation optoelectronic and magnetic devices. Besides, investigation of these properties in NRs is critically important from both fundamental and technological perspectives, as they represent ideal platforms for achieving extreme miniaturization in next-generation nanoelectronic devices, where quantum confinement effects can be harnessed for enhanced functionality beyond the limitations of conventional semiconductor technologies.

Consequently, in the second part of this work, we systematically investigate

how the magnetic properties evolve upon hole doping in MX NRs, elucidating the interplay between reduced dimensionality, electronic structure modulation, and spin distributions that are distinct from their 2D counterparts. We consider hole doping of MX NRs of 1T and 1H phases, with both zigzag and armchair edges, as well as with and without hydrogen passivation. Spin polarization energies of these structures are discussed by comparing their magnetization density profiles (MDPs) and electronic band structures. The considered hole doping range is from 1.5×10^{13} cm^{-2} to 1.35×10^{14} cm^{-2}.

The primary finding of this part of the thesis is that SPE in MX NRs can be significantly higher than in their 2D counterparts. The primary cause of this difference lies in the edge-localization of carriers in p-doped MX NRs as a result of the quantum confinement effect. Higher edge-localization leads to higher SPE. Such edge states are generally more pronounced in the case of UP-NRs, as passivation saturates the dangling bonds and reduces the edge effect. Furthermore, due to the structural symmetry of the 1H phase, its NRs exhibit stronger edge-localization in NRs, unlike the centrosymmetric 1T phase. In addition, the ANRs generally exhibit lower edge effects than ZNRs. Nevertheless, as these MX NR systems are considerably complex, various parameters can result in different behaviors. Herein, we aim to show correlations between edge-localization and high SPE, as well as additional factors that may come into play in each MX NR scenario with various combinations of parameters such as passivation, edge shape, phase, and atomic composition.

Chapter 2

Theoretical Background

2.1 Many-Body Schrödinger Equation and Born-Oppenheimer Approximation

In order to describe a nanoscale material quantum-mechanically, one must, in principle, solve the time-dependent Schrödinger equation for all electrons and nuclei. In the stationary case, the many-body Schrödinger equation is as follows:

$$\hat{H}\,\Psi_i(\mathbf{r},\mathbf{R}) \;=\; E_i\,\Psi_i(\mathbf{r},\mathbf{R}) \tag{2.1}$$

where $\mathbf{r} = (r_1,\ldots,r_{N_e})$ and $\mathbf{R} = (R_1,\ldots,R_N)$ denote electronic and nuclear coordinates, respectively, and $\hat{H}$ is the Hamiltonian

$$\hat{H} = \sum_{I=1}^{N} \frac{-\hbar^2}{2M_I}\nabla_I^2 + \sum_{i=1}^{N_e} \frac{-\hbar^2}{2m_e}\nabla_i^2 + \sum_{i<j} \frac{e^2}{|\mathbf{r}_i-\mathbf{r}_j|} + \sum_{I<J} \frac{Z_I Z_J e^2}{|\mathbf{R}_I-\mathbf{R}_J|} - \sum_{i,I} \frac{Z_I e^2}{|\mathbf{r}_i-\mathbf{R}_I|}\,. \tag{2.2}$$

Direct solution of Eq. (2.1) is only feasible for the smallest systems, due to the $3N_e + 3N$ degrees of freedom and the electron–electron correlations.

The Born–Oppenheimer approximation decouples electronic and nuclear motion by exploiting the large mass difference between them. One writes the total

wavefunction as

$$\Psi(\mathbf{r}, \mathbf{R}) \;=\; \Theta(\mathbf{R})\, \Phi(\mathbf{r}; \mathbf{R})\,, \tag{2.3}$$

and treats nuclei classically while solving the electronic problem at fixed $\mathbf{R}$. The electronic Hamiltonian becomes

$$\hat{H}_e = -\sum_i \frac{\hbar^2}{2m_e}\nabla_i^2 - \sum_{i,I} \frac{Z_I e^2}{|\mathbf{r}_i - \mathbf{R}_I|} + \frac{1}{2}\sum_{i \neq j} \frac{e^2}{|\mathbf{r}_i - \mathbf{r}_j|}\,, \tag{2.4}$$

and the total energy separates into kinetic, external (nuclear–electron), and interaction terms:

$$E = \hat{T} + \hat{V}_{\text{ext}} + \hat{V}_{\text{int}}\,. \tag{2.5}$$

Solving for $\Phi(\mathbf{r}; \mathbf{R})$ remains a many-electron problem, which motivates further approximation.

2.2 Density Functional Theory

Density Functional Theory (DFT) reformulates the electronic problem in terms of the three-dimensional electron density $\rho(\mathbf{r})$, rather than the many-electron $3N_e$-dimensional wavefunction (see Figure 2.1. All ground-state properties can, in principle, be obtained from $\rho(\mathbf{r})$.

2.3 Hohenberg–Kohn Theorems

The fundamental theoretical framework of DFT was established by Hohenberg and Kohn in their pivotal 1964 work [55], consisting of two main theorems. The first Hohenberg–Kohn theorem states that, for a given external potential $v(\mathbf{r})$, the ground-state density $\rho_0(\mathbf{r})$ uniquely determines $v(\mathbf{r})$ (up to an additive constant). Consequently, all observables are functionals of $\rho(\mathbf{r})$. The second theorem establishes a variational principle: there exists a universal energy functional $E[\rho]$ whose minimum at the true ground-state density yields the exact ground-state energy. However, these theorems do not tell us how to construct $E[\rho]$ in practice.

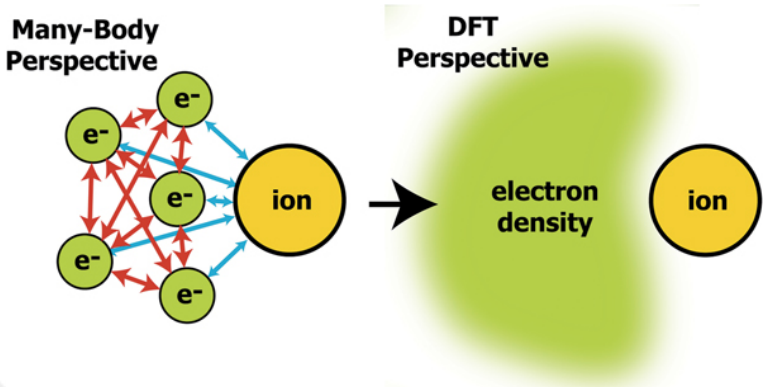

Figure 2.1: DFT reformulates the complex many-body electron problem by employing electron density as the fundamental variable, circumventing the need to solve for the complete many-electron wavefunction. Reproduced from [2] with permission from Springer Nature.

2.4 Kohn–Sham Equations

In 1965, Kohn and Sham introduced a fictitious non-interacting system that reproduces the true density [56]. The density is expressed as:

$$\rho(\mathbf{r}) = \sum_{i=1}^{N_s} |\psi_i(\mathbf{r})|^2 \tag{2.6}$$

and replaces the true kinetic energy by

$$T_s[\rho] = \sum_{i=1}^{N_s} \langle \psi_i | -\tfrac{\hbar^2}{2m_e} \nabla^2 | \psi_i \rangle \,. \tag{2.7}$$

The total energy functional becomes

$$E_{\mathrm{KS}}[\rho] = T_s[\rho] + \int \rho(\mathbf{r})\, v(\mathbf{r})\, \mathrm{d}^3 r + \frac{1}{2} \iint \frac{\rho(\mathbf{r})\, \rho(\mathbf{r}')}{|\mathbf{r} - \mathbf{r}'|}\, \mathrm{d}^3 r\, \mathrm{d}^3 r' + E_{\mathrm{xc}}[\rho] \,, \tag{2.8}$$

where $E_{\mathrm{xc}}[\rho]$ is the exchange–correlation (XC) functional. Stationary variation leads to the Kohn–Sham equations,

$$\left[-\frac{\hbar^2}{2m_e} \nabla^2 + v_{\mathrm{eff}}(\mathbf{r}) \right] \psi_i(\mathbf{r}) = \varepsilon_i\, \psi_i(\mathbf{r}) \,, \tag{2.9}$$

with

$$v_{\mathrm{eff}}(\mathbf{r}) = v(\mathbf{r}) + v_{\mathrm{H}}(\mathbf{r}) + v_{\mathrm{xc}}(\mathbf{r}) \,, \quad v_{\mathrm{H}}(\mathbf{r}) = \int \frac{\rho(\mathbf{r}')}{|\mathbf{r} - \mathbf{r}'|}\, \mathrm{d}^3 r', \quad v_{\mathrm{xc}}(\mathbf{r}) = \frac{\delta E_{\mathrm{xc}}}{\delta \rho(\mathbf{r})} \,. \tag{2.10}$$

These equations are solved self-consistently until $\rho(\mathbf{r})$ converges.

2.5 Exchange–Correlation Approximations

As the exact exchange–correlation (XC) functional is unknown except for the homogeneous electron gas, practical calculations employ approximations.

In the Local Density Approximation (LDA) [61], one uses the XC energy density of the uniform gas at each point,

$$E_{\mathrm{xc}}^{\mathrm{LDA}}[\rho] = \int \rho(\mathbf{r})\, \varepsilon_{\mathrm{xc}}^{\mathrm{HEG}}\big(\rho(\mathbf{r})\big)\, \mathrm{d}^3 r\,. \tag{2.11}$$

which often overbinds molecules and underestimates the band gaps.

Generalized Gradient Approximations (GGAs) [62] incorporate density gradients,

$$E_{\mathrm{xc}}^{\mathrm{GGA}}[\rho] = \int f\big(\rho, \nabla\rho\big)\, \mathrm{d}^3 r\,, \tag{2.12}$$

improving energetics and structures. In this study, we employ PBE functional [63], which is one of the most widely used GGA functionals.

We also utilize hybrid functionals, which mix a fraction of exact Hartree–Fock exchange with GGA exchange–correlation. A notable example is the HSE06 functional [64], which partitions the Coulomb kernel into short-range and long-range parts and replaces 25% fraction of the short-range GGA exchange by the exact exchange, while retaining GGA exchange at a long range. This screening reduces self-interaction errors and yields much improved electronic band dispersions and bandgaps in solids.

2.6 Pseudopotentials

Since core electrons vary rapidly near nuclei yet do not contribute significantly to bonding, one replaces the full nuclear plus core potential with a smooth pseudopotential acting only on valence electrons. Norm-conserving and ultrasoft pseudopotentials enforce orthogonality to core states while lowering plane-wave cutoffs [65].

On the other hand, the Projector Augmented-Wave (PAW) method transforms all-electron wavefunctions into smooth auxiliary ones plus atom-centered corrections, retaining full accuracy with moderate cutoffs [66]. Both of these methods aim to reduce the number of plane waves needed to expand valence states.

2.7 Plane-Wave Basis and k-Point Sampling

For periodic solids, Bloch's theorem allows each Kohn–Sham orbital to be written as

$$\psi_{n\mathbf{k}}(\mathbf{r}) = e^{i\mathbf{k}\cdot\mathbf{r}}\, u_{n\mathbf{k}}(\mathbf{r})\,, \quad u_{n\mathbf{k}}(\mathbf{r}+\mathbf{L}) = u_{n\mathbf{k}}(\mathbf{r})\,, \tag{2.13}$$

and $u_{n\mathbf{k}}$ is expanded in plane waves,

$$u_{n\mathbf{k}}(\mathbf{r}) = \sum_{\mathbf{G}} c_{n,\mathbf{k}+\mathbf{G}}\, e^{i\mathbf{G}\cdot\mathbf{r}}\,, \tag{2.14}$$

where $\mathbf{G}$ are reciprocal-lattice vectors. The infinite Brillouin-zone integral is replaced by a finite sum over a mesh of $\mathbf{k}$-points:

$$\frac{1}{\Omega}\int_{\mathrm{BZ}} F(\mathbf{k})\,\mathrm{d}^3k \;\approx\; \sum_{j} w_j\, F(\mathbf{k}_j)\,, \tag{2.15}$$

with weights w_j.

Γ-centered grids place a point at $\mathbf{k} = 0$ and sample symmetrically around it, which better preserves crystal symmetry and avoids spurious offsets in metallic or small-gap systems. Monkhorst–Pack grids can be shifted, but for layered or low-dimensional materials a Γ-centered mesh often yields faster convergence of total energies and forces.

In this thesis, we present results of DFT calculations executed using VASP (Vienna Ab initio Simulation Package) [67], which implements plane-wave basis sets under periodic boundary conditions.

2.8 Inverse Participation Ratio

First introduced in 1970 by Bell and Dean [68], the Inverse Participation Ratio (IPR) to this day remains a widely used quantitative measure of localization for a given distribution, such as wavefunctions or charge densities. For a normalized distribution $f(y)$ defined on a discrete or continuous domain, the IPR is defined as:

$$\text{IPR} = \int |f(y)|^4 \, dy \tag{2.16}$$

or, for a discrete set of points,

$$\text{IPR} = \sum_i |f_i|^4 \tag{2.17}$$

where f_i is the normalized value at site i and the normalization condition is

$$\sum_i |f_i|^2 = 1 \tag{2.18}$$

The IPR quantifies the degree of localization:

- For a completely delocalized (uniform) distribution over N sites, $f_i = 1/\sqrt{N}$, so IPR $= 1/N$.
- For a maximally localized distribution (all weight at a single site), $f_j = 1$ for some j, $f_{i \neq j} = 0$, so IPR $= 1$.

Thus, higher IPR values indicate stronger localization.

In our study, the IPR is utilized to quantify the degree of localization of the magnetization (carrier) distribution along the width of the hole-doped nanoribbons.

Chapter 3

Structural Properties: Width-dependent Phase Favorability

The structural properties of NRs are predominantly governed by edge configuration, width, crystallographic phase, and edge functionalizations, with hydrogen termination being one of the most widely utilized and energetically favorable for most systems [22, 69]. Experimental characterizations reveal edge reconstruction phenomena where pristine edges spontaneously reconstruct to minimize dangling bonds and edge energy [70]. It has been shown theoretically, using DFT calculations, that phase transitions to metastable or energetically unfavorable phases in 2D systems may occur in NRs due to intrinsic or external effects [52]. The most common causes for phase transitions in NRs include strain, chemical doping, and externally applied electric fields [52, 53]. Furthermore, it has been shown that phase transitions show reduced energy barriers in NRs compared to their 2D counterparts due to edge-facilitated nucleation processes [8, 71, 72]. The width-dependent phase preference enables controlled engineering of electronic and magnetic properties through dimensional confinement, broadening the spectrum of perspective applications of NRs [22].

Two-dimensional (2D) group III metal monochalcogenides (MXs, where M = Ga, In and X = S, Se) have attracted extensive interest owing to their multiple polymorphic phases, each exhibiting unique physical characteristics [23, 24, 25, 26, 27, 28, 29, 30]. In their ground state, these materials adopt a hexagonal (H) phase with D_{3h} symmetry, characterized by an X–M–M–X stacking sequence within the unit cell. However, first-principles studies [30, 32, 31] have shown that MXs can also exist in a metastable staggered T phase belonging to the D_{3d} point group. The T-phase energy lies very close to that of the H phase, separated by a barrier smaller than k_BT at room temperature, and differs only in the arrangement of the chalcogen atoms while retaining an otherwise similar structural framework (see Figure 1.1) [31].

The presence of promising characteristics such as the Mexican-hat-shaped valence band in 2D MXs has stimulated investigations of their 1D analogs [73, 74]. To date, however, most studies have focused exclusively on NRs derived from the 1H phase, leaving the 1T-phase NRs largely unexplored. In this chapter, we demonstrate that for both P-ZNRs and UP-ZNRs, the 1T-phase configuration remains thermodynamically favorable up to critical widths of approximately 23 nm, 31 nm, and 34 nm for GaS, GaSe, and InSe NRs, respectively. This pronounced stability of 1T ZNRs over their 1H counterparts arises from the absence of a built-in electric field in the 1T phase, which leads to increased formation energies in the polar 1H ZNRs. In contrast, in MX ANRs, both 1H and 1T phases are non-polar; in P-ANRs, the 1H phase is thermodynamically more favorable, while in UP-ANRs, the 1T phase is thermodynamically more favorable in the very narrow widths regime up to 3.3nm in the case of InSe UP-ANRs.

This chapter is partially based on our following publication: [1].

3.1 Computational Details

Density functional theory (DFT) calculations are performed using the Vienna Ab initio Simulation Package (VASP) [67]. We employ projector augmented-wave

(PAW) pseudopotentials [75, 66] in conjunction with the generalized gradient approximation of Perdew, Burke, and Ernzerhof [63, 76, 77], with spin polarization considered. Ribbons are placed in the x-y plane (see Figure 1.1), and a vacuum of 15 Å is considered along the non-periodic directions to eliminate interactions between periodic images. Geometry optimizations are carried out using a plane-wave kinetic energy cutoff of 500 eV, while Brillouin zone sampling is performed with a Γ-centered $10 \times 1 \times 1$ and $6 \times 1 \times 1$ k-point mesh is used for sampling the ZNRs and ANRs, respectively. The convergence criteria are set such that the total energy change between electronic steps does not exceed 10^{-7} eV, and the Hellmann–Feynman forces on each atom are reduced below 10^{-2} eV/Å.

3.2 Results and Discussion

Here, we denote N as the number of 2D monolayer unit cells composing each nanoribbon. We have examined MX ZNRs with N varying from 4 to 14 and ANRs with N ranging from 4 to 10. As described in Table A.1, our computed structural parameters and energy differences for the corresponding 2D MX systems are in excellent agreement with earlier studies [78, 31]. Moreover, upon increasing N, the lattice constants of the fully relaxed ZNRs and ANRs gradually approach those of the pristine 2D monolayer, indicated by dashed lines (see Figures A.1 and A.2).

Figure 3.1 depicts the dependence of the total ground-state energy difference between the 1H and 1T phases of MX ZNRs ($\Delta E = E_{1H} - E_{1T}$) on the ribbon width N. The first striking observation from this plot is that, in contrast to the corresponding $2D$ monolayers, ΔE remains positive for all investigated ZNR widths, signifying that the 1T phase is thermodynamically favorable. As N increases, UP-ZNRs exhibit a linear decline in ΔE, whereas in P-ZNRs, ΔE only begins to decrease after reaching a peak value. This trend is anticipated, since beyond a certain critical width, the 1H phase is expected to become more stable than the 1T phase (at $\Delta E < 0$).

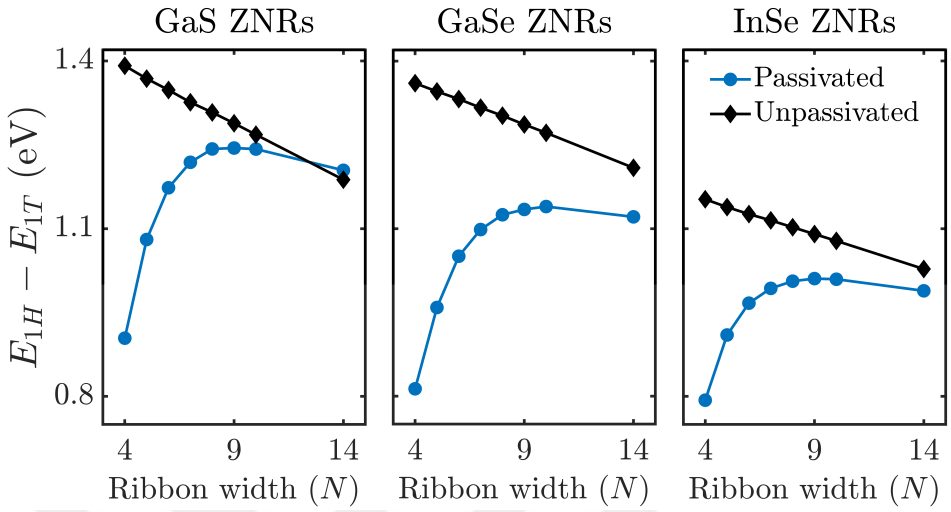

Figure 3.1: Energy difference between the 1H and 1T phases in passivated (blue circles) and unpassivated (black diamonds) ZNRs with respect to N. Lines are guides for the eye. Adapted from Aliyev et al. [1] under a CC BY license.

On the other hand, as can be seen from Figure 3.2, in MX ANRs ΔE is significantly smaller than in ZNRs, showing positive values only in the unpassivated cases, while in P-ANRs ΔE is negative even at very narrow ANR widths.

As demonstrated in Ref. [54], the critical ribbon width for the phase transition can be obtained by evaluating the formation energy of the NRs. For UP-NRs, the formation energy is defined by:

$$E_{form}(N) = E_r(N) - NE_{2D}, \tag{3.1}$$

where $E_r(N)$ denotes the total energy of the nanoribbon containing N unit cells, and E_{2D} represents the energy per formula unit of the corresponding two-dimensional monolayer. In the case of P-ZNRs (or ANRs), the energy equivalent to two (or four) hydrogen molecules is additionally subtracted on the right-hand side of Eq. 3.1. Thereafter, by examining the converged values of E^{1H}_{form} and E^{1T}_{form} as functions of N, one can extract the critical width N_c according to:

$$N_c = \frac{E^{1H}_{form} - E^{1T}_{form}}{E^{1T}_{2D} - E^{1H}_{2D}} \tag{3.2}$$

The formation energies with respect to N are shown in Figures 3.3 and 3.4,

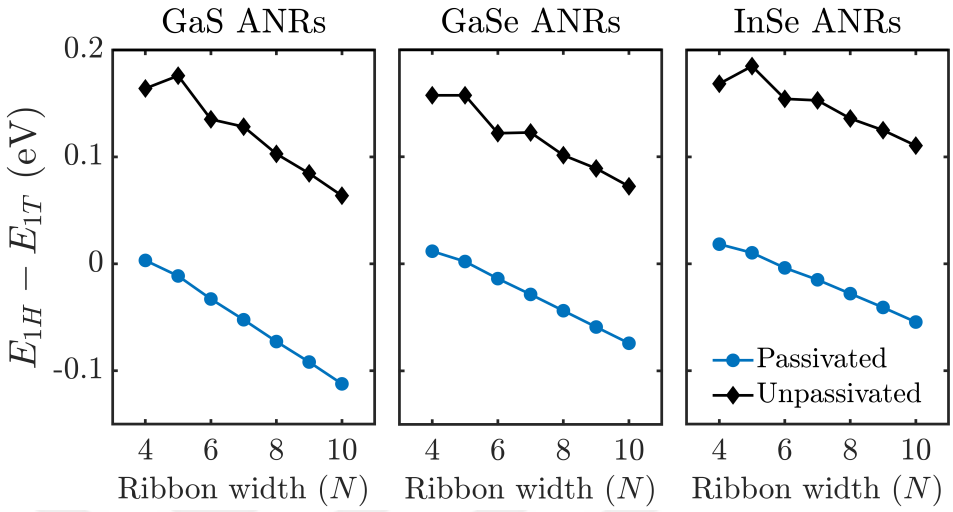

Figure 3.2: Energy difference between the 1H and 1T phases in passivated (blue circles) and unpassivated (black diamonds) ANRs with respect to N. Lines are guides for the eye.

where convergence with increasing N is evident. The energy values at the largest ribbon widths considered were utilized to determine E_{form}^{1H} and E_{form}^{1T}. The resulting critical widths N_c are listed in Table 3.1. For ZNRs, the smallest N_c is 72 (corresponding to 23 nm) for GaS P-ZNRs, whereas the largest N_c is 95 (34 nm) for InSe UP-ZNRs. Importantly, these predicted widths are within the reach of current fabrication techniques [79, 40, 45, 41], and are substantially greater than those reported for TMD nanoribbons, where the maximum critical width is 2.5 nm [54, 80]. On the other hand, for ANRs, 1T is more favorable only in unpassivated cases in very narrow widths of up to 3.3nm in the case of InSe ANRs.

The hydrogenation energies (E_H) shown in Figure 3.5 provide additional understanding of the nonlinear variation in ΔE for passivated ZNRs. While E_H for 1T ZNRs remains essentially invariant, 1H ZNRs exhibit a nonlinear dependence of ΔE that can be fitted by $\frac{\alpha}{N^2} + \beta$, as indicated by the dashed red curves in Figure 3.5. This nonlinearity in E_H originates from the behavior of E_{form} illustrated in Figure 3.3, where 1H-P-ZNRs display a nonlinear trend, whereas 1H-UP-ZNRs maintain an almost constant E_{form}. Furthermore, planar-averaged local potentials (V_{pal}), presented in Figures 3.6, A.3, and A.4, reveal another characteristic of

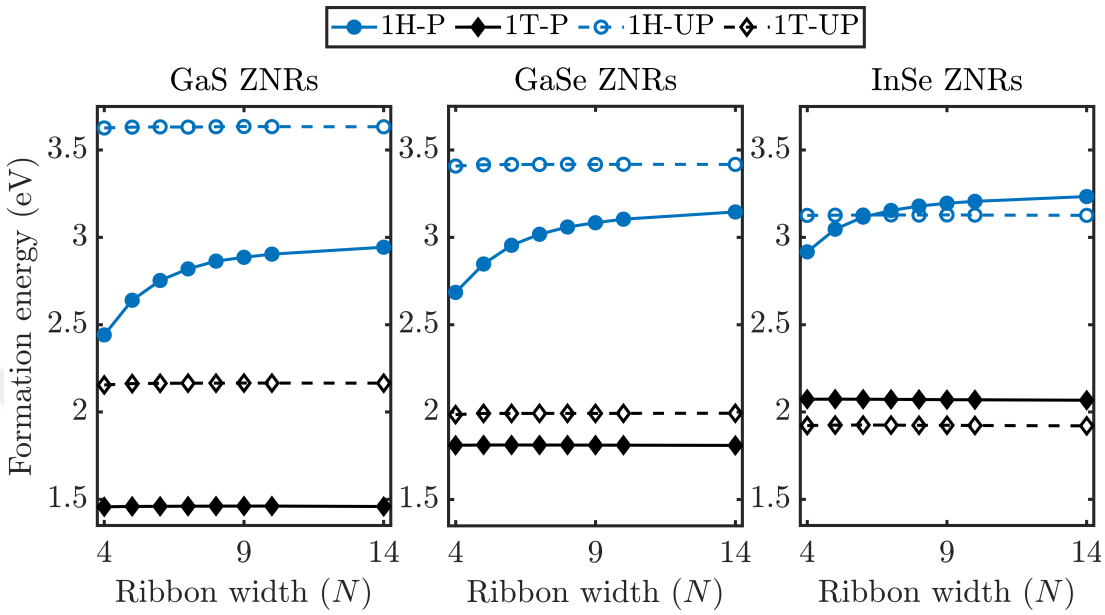

Figure 3.3: Calculated formation energies of MX ZNRs plotted against ribbon width. Solid Lines are guides to the eye. Adapted from Aliyev et al. [1] under a CC BY license.

1H-P-ZNRs. Across the ribbon width, V_{pal} exhibits oscillatory extrema of nearly constant magnitude for most ZNRs, with the exception of 1H-P-ZNRs, which display a near-linear progression of extrema, a phenomenon analogous to that observed in polar surfaces [81, 82] and nanoribbons [83].

Importantly, Figure 3.6 reveals a built-in electric field present exclusively in 1H ZNRs, which plays a crucial role in determining their thermodynamic stability. As theorized by Zhong et al. [84] in 2012 and confirmed experimentally next year by Kuiper et al. [85], the stability of ultrathin films is governed by the competition between the built-in electric field and reconstruction processes; as the number of layers decreases, non-polar thin films become energetically favored, compensating for residual electrostatic energy. In this context, we observe that non-polar MX ZNRs attain greater stability when their ribbon widths are sufficiently small. Of particular note, STEM images of few-layer 2D GaSe have demonstrated that, due to the presence of a built-in electric field, an H-to-T phase transition can occur, which has been exploited for ferroelectric switching [25].

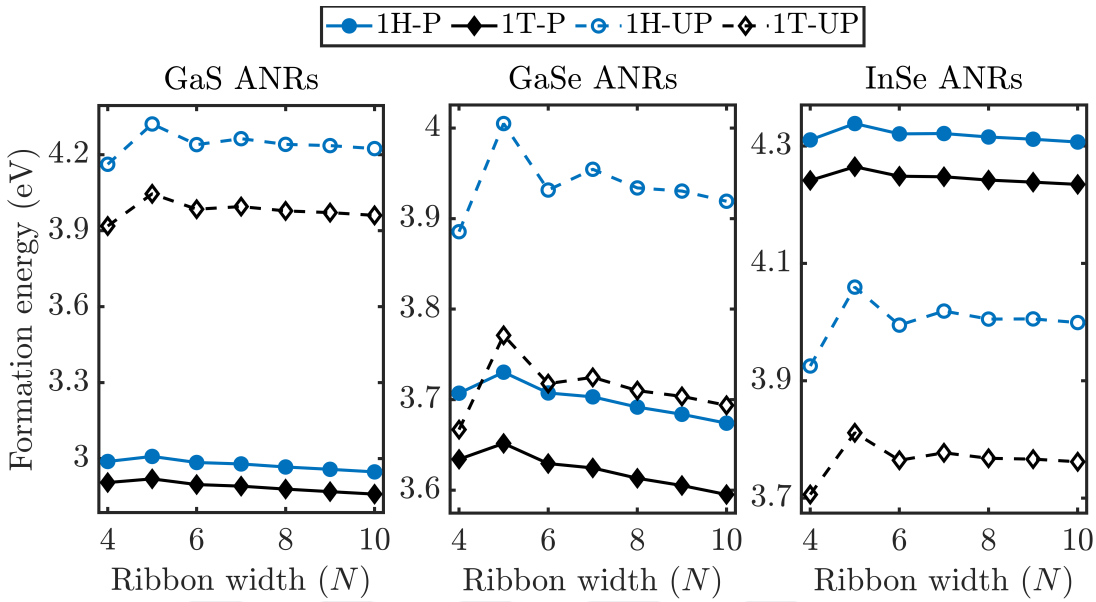

Figure 3.4: Calculated formation energies of MX ANRs plotted against ribbon width. Solid Lines are guides to the eye.

Consequently, the MX ANRs, which do not possess built-in potential between the edges, exhibit small ΔE for the UP-ANRs and negative ΔE for the P-ANRs, indicating the thermodynamic favorability of the 1H phase, similar to the 2D counterparts. Furthermore, they do not show $\frac{\alpha}{N^2} + \beta$ behavior of E_H, which is again in agreement with their V_{pal} profile. The E_H of ANRs show convergence to a certain value, except at very narrow widths where one may observe some oscillations. The width-dependent oscillations in energies observed in ANRs originate from quantum confinement effects that induce distinct electronic states at the edges, conforming to a characteristic periodicity. The differences in edge symmetry cause width-dependent variations in edge state decay lengths and charge redistributions. With increasing width, these edge effects become negligible, which is also observed in all our energy vs ribbon width figures. For example, similar phenomena are observed in AGNRs, where oscillations in formation energies and band gaps can be seen depending on the width. Nonetheless, unlike AGNRs, where oscillations are grouped in periods of 3, in MX ANRs, we observe periodicity of 2, which is likely due to the bilayer structure, which modifies the symmetry of ANRs.

Table 3.1: The calculated values of critical width in terms of N_c (defined in Eq. 3.2) where the crossover between the 1T and 1H phases occurs in MX ZNRs and ANRs.[a] Adapted from Aliyev et al. [1] under a CC BY license.

	ZNRs				ANRs	
	Unpassivated		Passivated		Unpassivated	
	N_c	W (nm)	N_c	W (nm)	N_c	W (nm)
GaS	73	23	72	23	13	2.1
GaSe	93	31	87	29	15	2.4
InSe	95	34	92	33	19	3.3

[a] The approximate width (W in nm) is calculated using the lattice constant of the corresponding 2D monolayer.

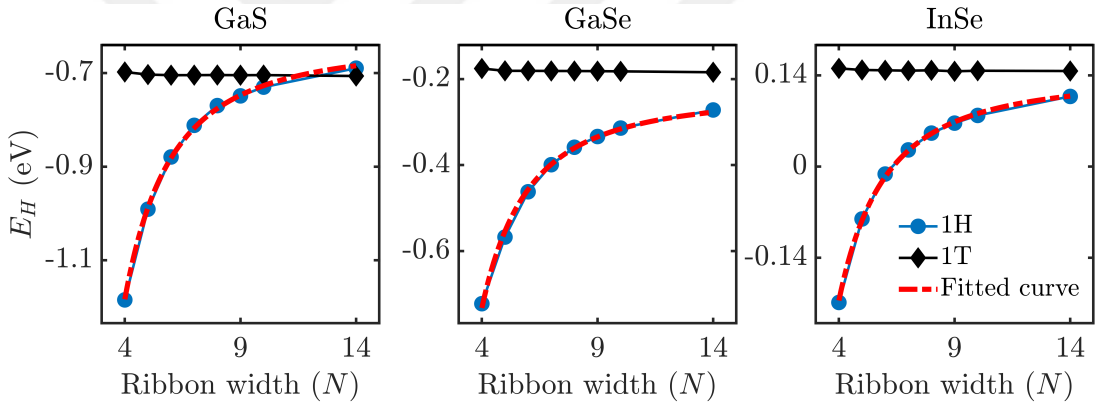

Figure 3.5: The calculated hydrogenation energies of 1T (black diamonds) and 1H (blue circles) MX ZNRs as a function of width. Solid lines are guides to the eye. The red dashed lines are $\frac{\alpha}{N^2} + \beta$ fits for describing the nonlinear behavior of 1H ZNRs. Adapted from Aliyev et al. [1] under a CC BY license.

In a related context, for MX ANRs at narrow widths, as shown in Figures 3.3 and 3.4, the E_{form} values increase when ANR N is odd, and decrease when N is even. Another noteworthy observation induced from E_{form} values is the relative stability of ZNRs to ANRs. One may notice that independent of atomic constituents, the UP-ZNRs(P-ZNRs) have lower E_{form} than UP-ANRs(P-ANRs). Furthermore, there is an increasing trend in (E_H) as the atomic number of the constituents in MX NRs increases (see Figure 3.5). In the case of InSe NRs, both ZNRs (see Figure 3.5) and ANRs (see Figure 3.7) show positive E_H, indicating that UP-NRs are more thermodynamically favorable than P-NRs.

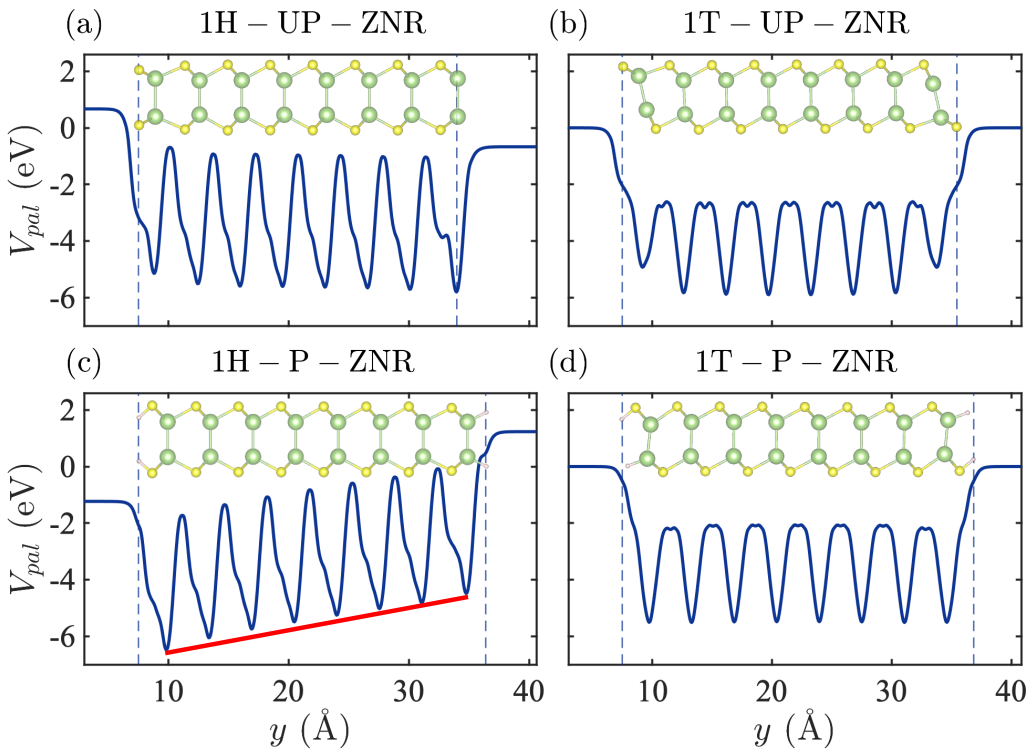

Figure 3.6: Planar average of the local electrostatic potential of (a) unpassivated 1H, (b) unpassivated 1T, (c) passivated 1H, and (d) passivated 1T $N = 8$ InSe ZNRs. Vertical dashed lines show the position of the first and last atom along the width of the NRs. Reproduced from Aliyev et al. [1] under a CC BY license.

In summary, DFT calculations were utilized to investigate the influence of ribbon width on the structural and electronic properties of both hydrogen-passivated and pristine MX zigzag and armchair nanoribbons. The principal outcome is the identification of a width-induced transition between the 1T and 1H polymorphs. Unlike the corresponding infinite monolayers, where the 1H phase is energetically preferred, in MX ZNRs, the nonpolar 1T configuration becomes thermodynamically more stable when the ribbon width falls below a critical value. This reversal of phase stability is a consequence of the competition between the intrinsic electric field of the ZNRs in the 1H phase and atomic reconstruction effects. The critical widths at which the 1T phase overtakes the 1H phase span from 23 nm for GaS to 34 nm for InSe ZNRs, dimensions that are accessible using contemporary fabrication methodologies. On the other hand, for ANRs, 1T is more favorable only in unpassivated cases in very narrow widths of up to 3.3nm in the case of

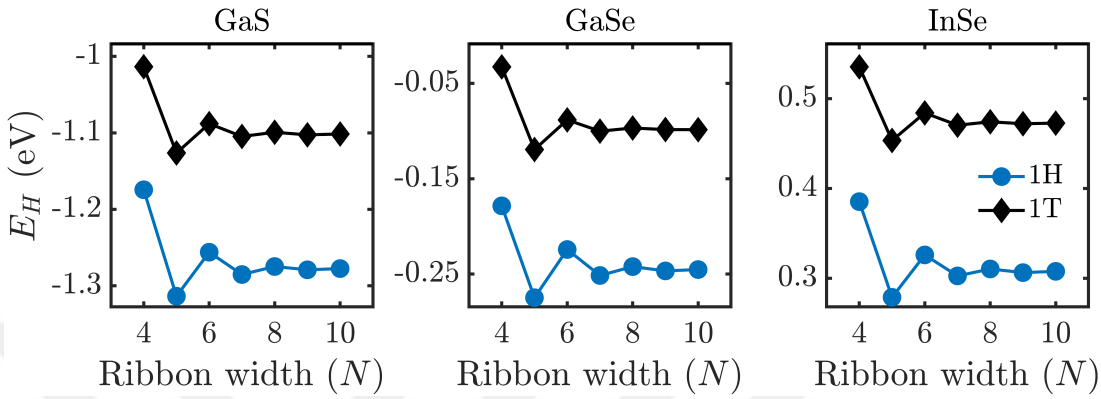

Figure 3.7: The calculated hydrogenation energies of 1T (black diamonds) and 1H (blue circles) MX ANRs as a function of width. Solid lines are guides to the eye.

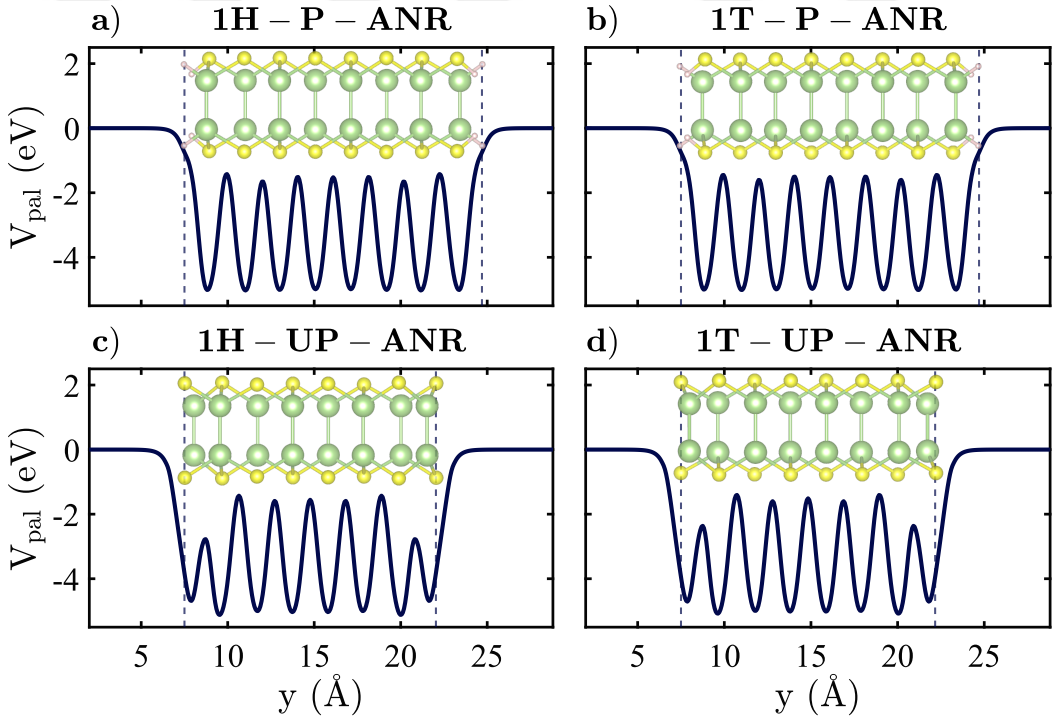

Figure 3.8: Planar average of the local electrostatic potential of (a) unpassivated 1H, (b) unpassivated 1T, (c) passivated 1H, and (d) passivated 1T $N = 8$ InSe ANRs. Vertical dashed lines show the position of the first and last atom along the width of the NRs.

InSe ANRs.

The origin of the difference between ZNRs and ANRs lies in their corresponding symmetries. Upon lateral confinement of 2D monolayer, polar M-X bonds are broken in MX NRs. However, the 1H ZNRs exhibit a non-centrosymmetric crystal structure with distinct edge terminations, producing uncompensated polar bonds, resulting in an intrinsic electrostatic potential gradient across the NR width, and creating localized charge distributions at opposing edges and increasing NR formation energy. Conversely, 1T phase ZNRs maintain inversion symmetry, which cancels electrostatic potential effects. The centrosymmetric configuration ensures that for each polar bond vector, a symmetrically equivalent counterpart exists with equal magnitude but opposite direction, yielding zero net dipole moment. Finally, in the case of ANRs, even 1H possesses inversion symmetry. Hence, there is no built-in potential between the edges, and ΔE only depends on edge effects, explaining the slight favorability of 1T phase in UP-ANRs where some edge effects are present. And upon passivation, the edge effects diminish, making the 1H phase more favorable.

Chapter 4

Electronic Properties of Undoped Nanoribbons

The electronic properties of NRs emerge as direct manifestations of their structural configurations. While the preceding chapter established the fundamental structural characteristics of these quasi-1D systems, their electronic behavior exhibits profound structure-property correlations that are of utmost interest. Edge termination (zigzag vs. armchair), ribbon width, chemical composition, and passivation state collectively dictate electronic band structures, magnetism, and transport capabilities [22]. Notably, structural confinement induces quantum size effects absent in bulk counterparts, generating unique electronic states localized at edges. However, passivation can fundamentally alter these localized states, causing charge redistribution by saturating the dangling bonds at the edges [69]. Based on first-principles calculations, one can study how the aforementioned structural modifications affect the charge density and electronic properties of NRs, and determine how to exploit them for use in advanced nanoelectronic devices.

Up to now, research efforts have focused exclusively on the electronic characteristics of MX nanoribbons in the 1H phase. Several theoretical works have

revealed compelling electronic and magnetic behaviors in these systems, for instance, the emergence of intrinsic ferromagnetism (FM) in GaS nanoribbons with zigzag termination (ZNRs) [47, 48]. Remarkably, this FM ordering in GaS ZNRs remains robust under both tensile and moderate compressive strains, with an antiferromagnetic (AFM) configuration only appearing under substantial magnitudes of compressive stress [57]. Furthermore, passivation studies on 1H MX NRs revealed edge-configuration-dependent electronic modifications, manifesting distinct effects according to ribbon width and edge termination geometry. The GaS and InSe ZNRs are reported to remain metallic and magnetic even after passivation with hydrogen, except at very narrow widths ($N \leq 4$) [49, 86, 58]. In contrast, both UP- and P-ANRs remain nonmagnetic semiconductors at all widths studied with even-odd dependence: increasing for odd N, and decreasing for even N. Furthermore, upon passivation, these ANRs exhibit an increase in bandgap values by at least 1eV [49, 86].

While prior investigations have focused almost exclusively on the 1H polymorph, our first-principles calculations established that the 1T phase is, in fact, thermodynamically favored in NRs below a certain critical width. Accordingly, this chapter is devoted to a comprehensive study of these stable 1T-phase ZNRs, with particular emphasis on their electronic properties and a direct comparison to both the corresponding 2D monolayer sheets and the well-studied 1H-phase NRs. We find that, unlike 1H-phase ZNRs, which typically exhibit edge-induced magnetism and metallic behavior, the 1T-phase ZNRs are inherently nonmagnetic semiconductors, regardless of width and passivation. In contrast, the electronic spectra of ANRs remain essentially unchanged between the 1H and 1T phases, a consequence of the preserved symmetry of the armchair edges, and the absence of the built-in potential. Finally, we demonstrate that hydrogen passivation of either zigzag or armchair edges in the 1T NRs uniformly increases the bandgap by saturating dangling bonds and diminishing the edge states.

This chapter is partially based on our following publication: [1].

4.1 Computational Details

For the electronic band structure calculations, we employed the same projector augmented-wave pseudopotentials within the Perdew-Burke-Ernzerhof generalized gradient approximation [63, 76, 77] used for structural optimization with spin polarization considered. Self-consistent calculations were performed with the energy cutoff of 500 eV for the plane-wave basis and k-point meshes of Γ-centered $10 \times 1 \times 1$ and $6 \times 1 \times 1$ for sampling the Brillouin zone (BZ) of ZNRs and ANRs, respectively. The convergence tolerance for the total energy of the system is set to be less than 10^{-7} eV. Non-self-consistent band structure calculations utilized a more dense $60 \times 1 \times 1$ k-point sampling along the periodic direction to accurately resolve the band dispersion.

For selected NR widths, we implemented the screened hybrid functional HSE06 [87] to confirm the observed band gaps and dispersions obtained using PBE. Due to its significant computational cost, HSE06 calculations were feasible only for narrow-width ribbons within available computational resources. The HSE06 functional is constructed by mixing 25% of the Fock exchange at short range with 75% of the PBE exchange at long range and 100% of the PBE correlation. This approach provides more accurate electronic structure predictions, particularly for systems with localized states.

4.2 Results and Discussion

The existence of an intrinsic potential significantly influences not only the structural but also the electronic characteristics of NRs. Previous investigations have demonstrated that the application of an external electric field to graphene and hexagonal boron nitride NRs and nanotubes induces a Wannier–Stark (WS)-like phenomenon, which causes displacement and splitting of degenerate electronic bands, a reduction in band gap, and ultimately drives semiconductor-to-metal transitions [88, 89, 90, 91, 92, 93]. In our study, we find that polar MX 1H

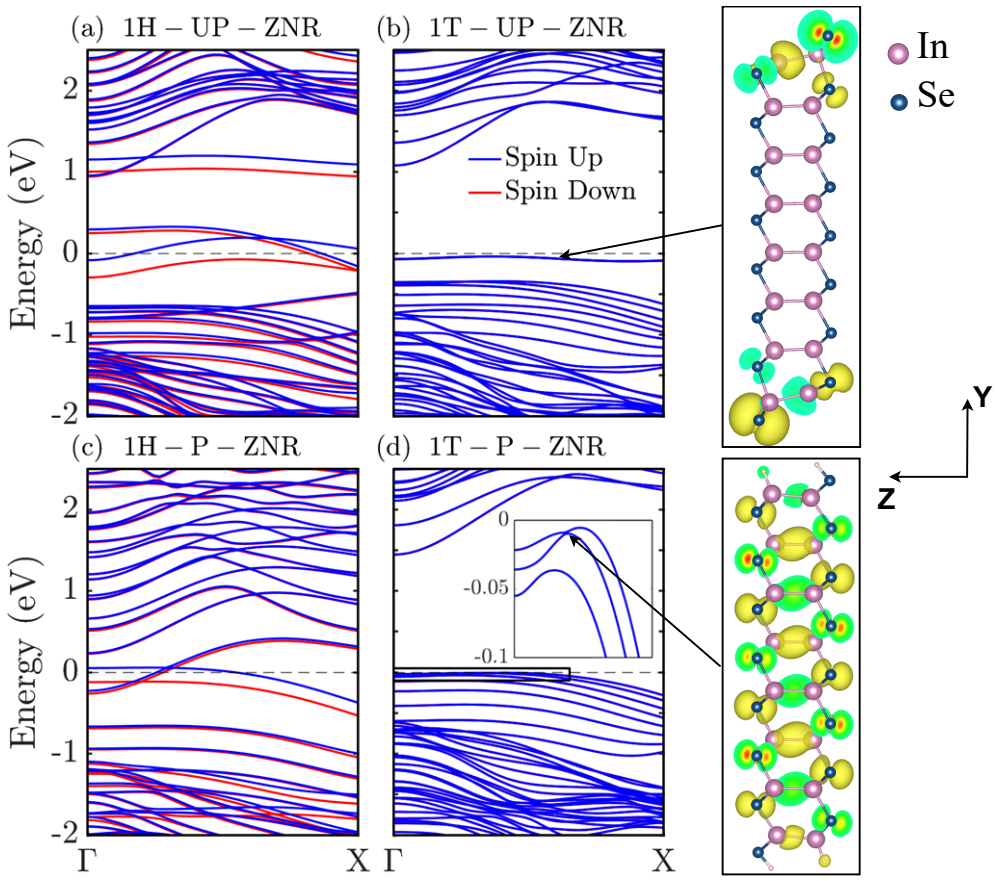

Figure 4.1: Spin-polarized band structures of (a) unpassivated 1H, (b) unpassivated 1T, (c) passivated 1H and (d) passivated 1T $N = 8$ InSe ZNRs with magnified view of top valence bands in the inset. The callout figures depict the partial charge distribution summed over all k-points of the two highest valence bands. Adapted from Aliyev et al. [1] under a CC BY license.

ZNRs exhibit metallic band dispersion even after hydrogen passivation, consistent with earlier reports [50, 49, 57, 47, 58, 48]. In contrast, nonpolar MX 1T ZNRs maintain a finite band gap irrespective of their passivation with hydrogen or their width (see Figures 4.1, A.5, A.6, and 4.3). A direct comparison between the electronic band dispersions of InSe 1H and 1T ZNR8s and those of their 2D monolayer supercells of matching dimensions (depicted in Figure 4.2) reveals a WS-like splitting of degenerate bands for 1H-P-ZNR8, one can recall that these NRs exhibit a ladder-like V_{pal} profile across the ribbon width (see Figure 3.6(c)). Other nanoribbons, however, show only minor lifting of band degeneracy observed in 2D due to structural distortions arising from quantum confinement.

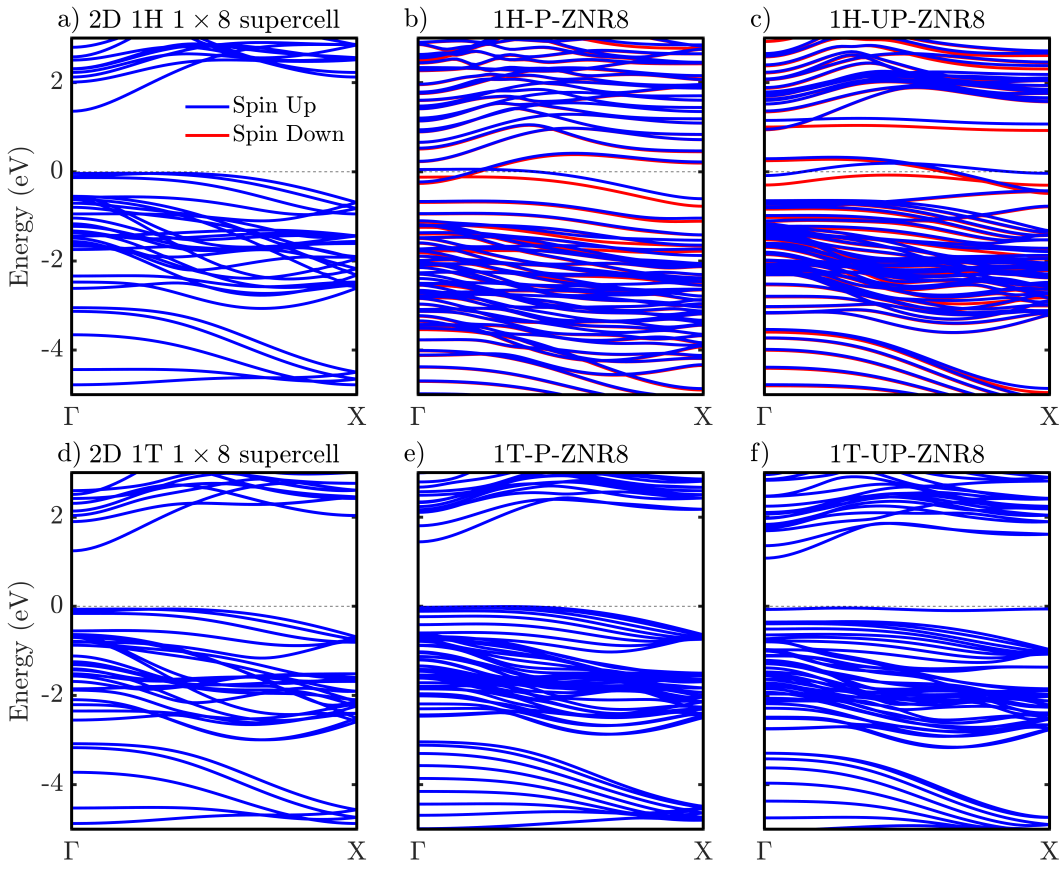

Figure 4.2: Spin-polarized band structures of InSe a) 2D 1H 1 × 8 supercell, b) 1H-P-ZNR8, c) 1H-UP-ZNR8, d) 2D 1T 1 × 8 supercell, e) 1T-P-ZNR8, and f) 1T-UP-ZNR8. Adapted from Aliyev et al. [1] under a CC BY license.

Furthermore, as shown in Figure 4.3 the band gaps of 1T-P-ZNRs show a decreasing trend that converges to 2D monolayer band gaps as the width increases, while the band gaps of UP-ZNRs exhibits no substantial width dependence. On top of it, similar to the 2D counterparts, 1T ZNRs possess a Mexican-hat-shaped top valence band, which is known to result in van Hove singularities (VHS) in the electronic density of states (DOS), leading to enhanced magnetic instabilities and potential ferromagnetic ground states under specific conditions of charge doping or applied electric field. Furthermore, as depicted in Figures 4.1 (b), A.5 (b), and A.6 (b), 1T-UP-ZNRs exhibit a nearly flat, edge-localized top valence band. Notably, as we demonstrated in the previous chapter, the E_H of InSe ZNRs is positive (see Figure 3.5), indicating the possibility of 1T InSe ZNRs formation without hydrogen passivation. To address the inherent deficiencies

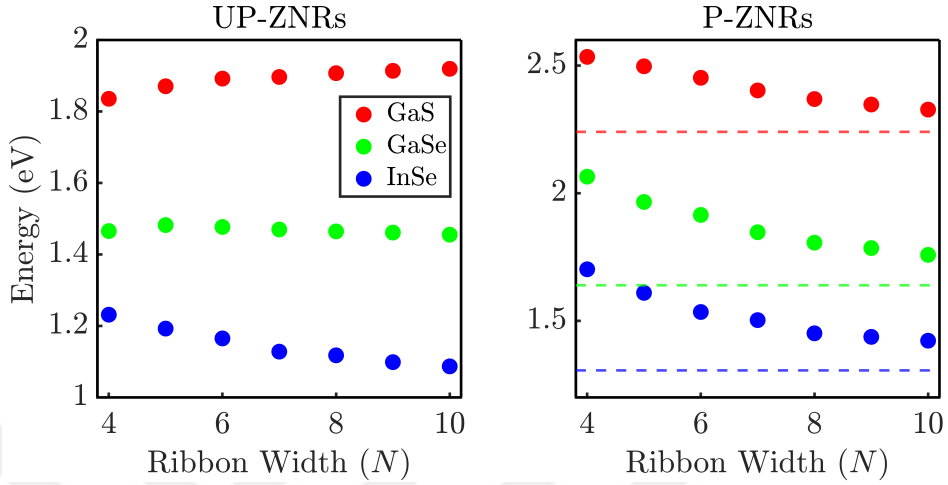

Figure 4.3: Variation of the bandgap of 1T MX ZNRs with ribbon width. Dashed lines represent the band gaps of 2D MXs, and the symbols represent the 1T ZNRs. Colors are consistent to indicate the respective materials. Adapted from Aliyev et al. [1] under a CC BY license.

in PBE-derived electronic band structures, we supplemented our computational analysis with the more rigorous HSE06 hybrid functional methodology. As depicted in Figure A.7, the obtained band dispersions from HSE06 calculations for 1T-ZNRs reveal remarkable consistency with their PBE counterparts in both 1T-UP and 1T-P configurations. However, the HSE06 functional systematically shifts the conduction bands to higher energies, increasing the bandgap magnitude by approximately 0.8eV, resulting in band gaps of about 1.9eV and 2.3eV for 1T-UP-ZNR5 and 1T-P-ZNR5, respectively.

On the other hand, in the case of MX ANRs, all structures, regardless of phase, passivation, and width, are observed to be nonmagnetic semiconductors. This fundamental difference originates from the intrinsic structural properties of ANRs. As described in the previous chapter, unlike ZNR counterparts, ANRs inherently possess inversion symmetry even in the 1H phase, thereby neutralizing the effect of broken polar bonds and eliminating any net built-in potential. This symmetry-induced phenomenon is unambiguously demonstrated in the electronic band structures and partial charge density distributions presented in Figure 4.5. The bandgaps of 1T ANRs depicted in Figure 4.4 display characteristic oscillatory behavior, with amplitudes increasing at even N and decreasing at odd N values,

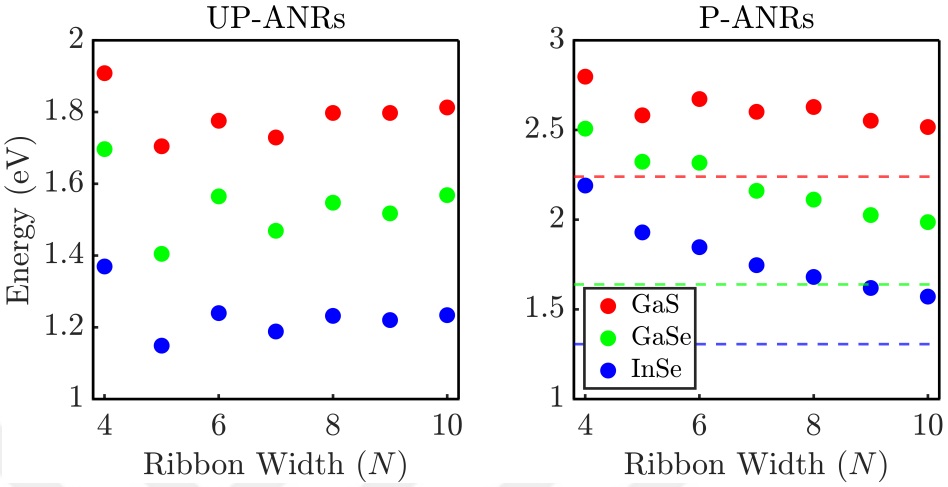

Figure 4.4: Variation of the bandgap of 1T MX ANRs with ribbon width. Dashed lines represent the band gaps of 2D MXs, and the symbols represent the 1T ZNRs. Colors are consistent to indicate the respective materials.

before converging at larger widths. Analogous to their ZNR counterparts, the 1T-P-ANR bandgaps demonstrate a monotonic decreasing trend asymptotically approaching the 2D monolayer bandgap values, independent of elemental composition. This convergence behavior represents a universal quantum confinement effect in passivated NR structures, with the electronic properties systematically evolving toward bulk-like characteristics as the width increases. Notably, ANRs lack the characteristic MHS dispersion in the topmost valence band that is prevalent in 1T ZNRs. However, they do exhibit considerable band flattening, particularly pronounced in 1H-UP-ANRs, which display the most spatially localized edge states among all ANR configurations due to their unique symmetry properties, as evidenced by the partial charge density maps in Figure 4.5(a). Furthermore, the passivation process effectively saturates dangling bonds, substantially diminishing the edge states in both 1H and 1T UP-ANRs, providing direct visualization of the electronic structure modification mechanism.

In summary, while 1H-ZNRs remain magnetic and metallic irrespective of hydrogenation, MX 1T-P-ZNRs exhibit a top valence band with a Mexican-hat dispersion analogous to that observed in the corresponding 2D monolayer structures, and their electronic band gaps decrease toward the values in 2D counterparts. These features of 1T-NRs make them a highly adaptable platform for

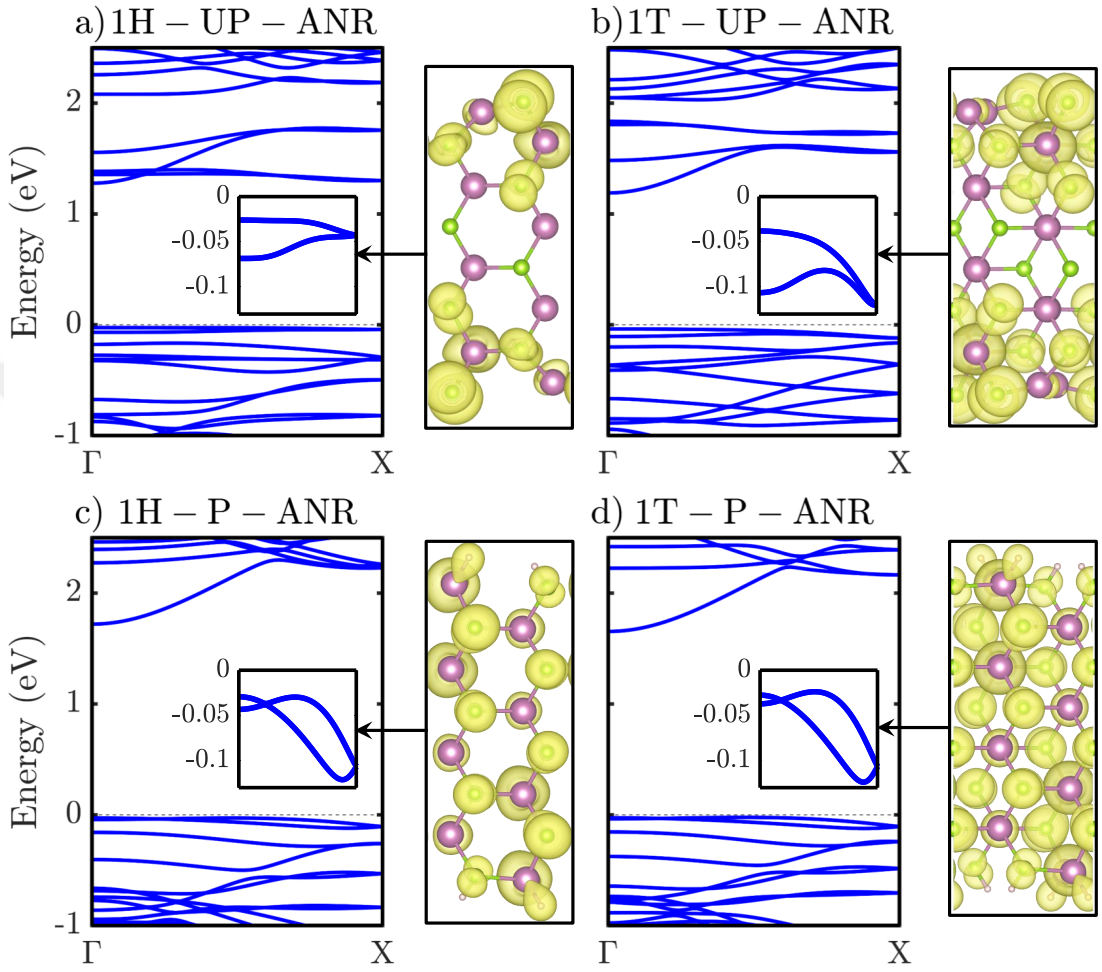

Figure 4.5: Spin-polarized band structures of (a) unpassivated 1H, (b) unpassivated 1T, (c) passivated 1H and (d) passivated 1T $N = 8$ InSe ANRs with magnified view of top valence bands in the inset.

thermoelectric and optoelectronic applications. Moreover, the positive hydrogenation energies combined with nearly flat valence band maxima make InSe 1T-UP-ZNRs promising candidates for spintronic and thermoelectric devices. In contrast, all MX ANRs are nonmagnetic semiconductors without the MHS dispersion in the topmost valence band. The bandgaps of MX 1T-ANRs display an oscillatory trend due to edge symmetry dependence on N, which decreases with increasing N. Similar to 1T-P-ZNRs, band gaps of 1T-P-ANRs also show a downward trend asymptotically approaching 2D monolayer values with increasing width. These results show that ribbon dimensionality and edge structure directly control the electronic and magnetic properties of MX NRs. One can predictably

adjust bandgaps, magnetism, and charge-carrier behavior by choosing the phase (1H or 1T), edge orientation (zigzag or armchair), and applying edge passivation. This provides a clear pathway for designing MX NRs in nanoelectronic and spintronic devices.

Chapter 5

Tunable Magnetization and Half-Metallicity via Hole Doping

Over the last decade, various materials have been investigated for utilization in the emerging field of spintronics, where charge and electron spin, along with their magnetic moments, are harnessed for information processing and storage [94]. This approach enables more energy-efficient devices with non-volatile memory capabilities. As technology advances toward miniaturization, the development of low-dimensional materials with tailored spin properties has become a major research focus [95]. Doping is a widely used method to induce new electronic and spintronic properties [3, 96]. As low-dimensional materials are often fragile, electrostatic doping (ED) using field-effect transistors (FETs) is now preferred over substitutional doping, since ED does not introduce defects and allows reversible and finely tunable control of the doping level, ensuring a prolonged lifetime of the designed devices [96].

Given the complexity and cost of experimental trial and error in designing such spintronic materials, numerous theoretical studies have employed DFT to investigate and predict low-dimensional materials, that could be potential candidates for spintronic applications. In a pioneering study in this field by Cao et al. [3], the electrostatic hole doping in the GaSe 2D monolayer was simulated by

reducing the total number of electrons and compensating it with a jellium background. It was shown that hole doping results in spin splitting and the emergence of itinerant magnetism persisting in a wide range of carrier densities, as well as half metallicity, meaning that only one spin channel crosses the E_f, leading to spintronic properties. The underlying reason for such properties is MHS of the topmost valence band, as it results in VHS (see Figure 5.1) in the DOS near E_f that, in turn, leads to ferromagnetic instabilities. In subsequent studies, it has been shown that such behavior in 2D materials upon hole doping is characteristic of materials with MHS electronic band structures, as in the competition between exchange and kinetic energies in systems with sharp singularity in DOS, the kinetic energy quenches, while exchange interaction is enhanced, resulting in spin splitting.

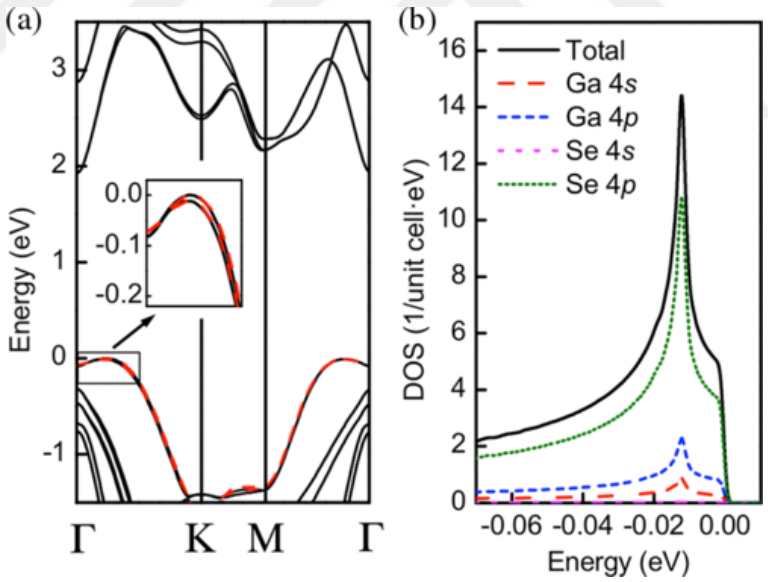

Figure 5.1: a) Electronic band-structure of undoped 2D GaSe monolayer with characteristic Mexican-hat-shaped topmost valence band. b) van Hove singularity in the corresponding DOS. Reproduced with permission from [3] Copyright (2015) by the American Physical Society.

Consequently, in recent years, researchers have been directed toward investigating hole doping implications on electronic and magnetic properties in NRs. Employing DFT calculations, Gao and Yang [60] demonstrated that narrow dihydrogenated GZNRs exhibit robust itinerant magnetism and half-metallicity upon electrostatic hole doping in the carrier density range of about 10^{13} cm^{-2}, with

spin-polarization energies (SPE) up to 17 meV/carrier. In addition, they similarly studied hole doping of mono- and di-hydrogenated GANRs, reporting once again itinerant magnetism and half-metallicity, although with lower SPE values than in the case of GZNRs, reaching up to about 12 meV/carrier. The authors noted that the SPE decreases with increasing width of NRs, as quantum confinement effects diminish. Notably, these values are significantly higher than in the pioneering study by Cao et al. [3], where the maximum observed SPE in 2D GaSe was approximately 3 meV/carrier. In a recent study by Ma et al. [97], hole doping of chevron GNRs (CGNRs) under an in-plane transverse electric field has been investigated using DFT calculations. The authors demonstrated that the applied electric field causes the collapse of valence and conduction bands into pairs of ultra-flat isolated π-bands, which lead to ferromagnetic instability, and upon hole doping, these bands undergo exchange splitting, resulting in half-metallicity. Authors highlighted that holes are distributed in these CGNRs at protrusions along the edges of the NR, creating a ferromagnetic, one-dimensional spin-1/2 chain along the ribbon length.

In this chapter, based on spin-polarized DFT calculations, we explore hole doping implications in MX NRs of 1T and 1H phases, with zigzag and armchair edges, as well as with (P-NRs) and without (UP-NRs) hydrogen passivation. The trends in SPE of these structures are analyzed by building correlations between real-space hole distributions along the width of NRs and corresponding electronic band dispersions. The considered hole doping range is from 1.5×10^{13} cm^{-2} to 13.5×10^{13} cm^{-2}, which lie within the experimentally achievable range for low-dimensional materials using state-of-the-art gating techniques.

Our work demonstrates that SPE in hole-doped NRs can be significantly higher than in their 2D counterparts, even at small carrier densities. The primary cause of this difference lies in the edge-localization of carriers in hole-doped MX NRs as a result of the quantum confinement effect. Higher edge-localization leads to sharper VHS near E_f in DOS and, hence, higher SPE. Such edge states are generally more pronounced in the case of UP-NRs, as passivation saturates the dangling bonds and reduces the edge effect. Furthermore, due to the absence of the inversion symmetry of the 1H phase, it exhibits stronger edge-localization in

NRs, unlike the centrosymmetric 1T phase. However, as mentioned previously, the 1H ZNRs are non-magnetic semiconductors only upon hydrogen passivation and at a very narrow width of up $N = 4$ and are less thermodynamically favorable than 1T ZNRs. In addition, we show that the ANRs generally exhibit lower edge localization effects than ZNRs, leading to lower SPE than NRs of comparable size. Finally, we illustrate a consistent correlation between SPE and valence band maximum (VBM) trends across all MX NRs considered. At carrier densities where SPE exhibits an increasing trend, the spin-up VBM shifts upwards, while the spin-down VBM shifts downwards; on the contrary, at certain carrier densities where SPE starts to reduce, the spin-down VBM starts to shift upwards. We attribute this behavior to the amount of DOS being shifted with every doping, which alters the balance between exchange and kinetic energy contributions. Initially, only the spin-up band is being shifted, as its top section contains high DOS due to the Mexican-hat shape or flatness, leading to strong exchange splitting. As doping increases and at a critical carrier density, that high DOS section is entirely above the E_f; from this point, the spin-down bands start to shift upwards as well, and we see a downward trend in SPE.

5.1 Computational Details

We employ spin-polarized DFT with projector augmented-wave pseudopotentials [75, 66] within the generalized gradient approximation of Perdew, Burke, and Ernzerhof [63, 76, 77]. Ribbons are placed in the x-y plane (see Figure 1.1), and a vacuum of 15 Å is considered in non-periodic directions to eliminate interactions with images. Electrostatic hole doping is achieved by removing electrons from the unit cell and compensating with a uniform jellium background of opposite charge to preserve neutrality. The structures are fully relaxed at every doping density using a kinetic energy cutoff of 500 eV for the plane-wave basis and a Γ-centered $10 \times 1 \times 1$ and $6 \times 1 \times 1$ k-point mesh for sampling the Brillouin zone (BZ) of ZNRs and ANRs, respectively. The convergence tolerance for the total energy of the system is set to be less than 10^{-7} eV, and the Hellmann-Feynman

forces are minimized to be less than 10^{-2} eV/Å. To obtain well-converged energies and magnetic moments in doped structures, we sample the Brillouin zone with dense Γ-centered $32 \times 1 \times 1$ and $20 \times 1 \times 1$ k-point mesh for ZNRs and ANRs, respectively, and apply a Gaussian smearing of 0.001 eV for the electronic occupations.

In accordance with [3], the SPE is defined as the total energy difference between the hole-doped nonmagnetic (spin-unpolarized) and ferromagnetic (spin-polarized) configurations, normalized by the number of doped carriers.

$$SPE = \frac{E_{\mathrm{NM}} - E_{\mathrm{FM}}}{n_{\mathrm{carriers}}} \tag{5.1}$$

In this formulation, the SPE serves as a quantitative measure of ferromagnetic stability: a larger (positive) SPE corresponds to a more stable ferromagnetic state.

5.2 Results and Discussion

In this section, we begin by examining hole-doping effects in the 2D parent materials and then proceed with their corresponding NRs. The analysis in each subsection starts from relatively simple MX systems and then proceeds to increasingly complex ones as additional factors emerge affecting magnetization and SPE.

5.2.1 2D monolayers

In agreement with previous reports [3, 59], upon hole doping of 2D MXs, namely InSe and GaSe, we observe exchange splitting of the topmost valence bands, which leads to half-metallicity and itinerant magnetization. The highest SPE magnitudes for 2D InSe and GaSe are approximately 11 and 7 meV/carrier,

respectively, as depicted in Figure A.8. Notably, the structural differences of 1H and 1T phases have negligible effect on magnetization and SPE in 2D MX structures, as the hole distributions are uniform across the structure, contrary to 1D NRs, that we demonstrate in the following subsections. Furthermore, as can be seen in Figure A.9, in 2D upon, hole doping, the bands exhibit rigid shift without noticeable deformations and changes in bandwidths.

5.2.2 ZNRs

In this section, various structural combinations of ZNRs are examined for comparative analysis and illustration of underlying mechanisms of hole doping. However, it is crucial to note that the structural properties described in Section 2 remain applicable: the 1T phase is thermodynamically more favorable than the 1H phase for all MX ZNRs till critical width N_c. Furthermore, InSe ZNRs are thermodynamically more stable in UP configuration, unlike GaSe and GaS ZNRs. Consequently, the primary emphasis is placed on InSe 1T-UP-ZNRs and GaSe 1T-P-ZNRs.

5.2.2.1 ZNRs with strong edge-localization: 1T-UP and 1H-P

In UP-ZNRs, the highest SPEs among considered NRs are observed, reaching magnitudes of about 38 meV/carrier at $p = 10.5 \times 10^{13}\ cm^{-2}$ in the case of InSe 1T-UP-ZNR6, which is about a fourfold increase in SPE compared to its 2D counterpart (see Figure A.10). Notably, in the case of GaSe 1T-UP-ZNR6, the SPE reaches about 32 meV/carrier at $p = 10.5 \times 10^{13}\ cm^{-2}$ (see Figure A.11), which is about a sixfold increase in SPE compared to its 2D counterpart. As can be seen from magnetization profiles of InSe 1T-UP-ZNR6 in Figure 5.2 (c), carriers in 1T-UP-zNRs are strongly localized at the edges of NRs in the considered doping range. Consequently, we observe itinerant magnetism in practically all considered doping densities, as shown in Figure 5.2 (b).

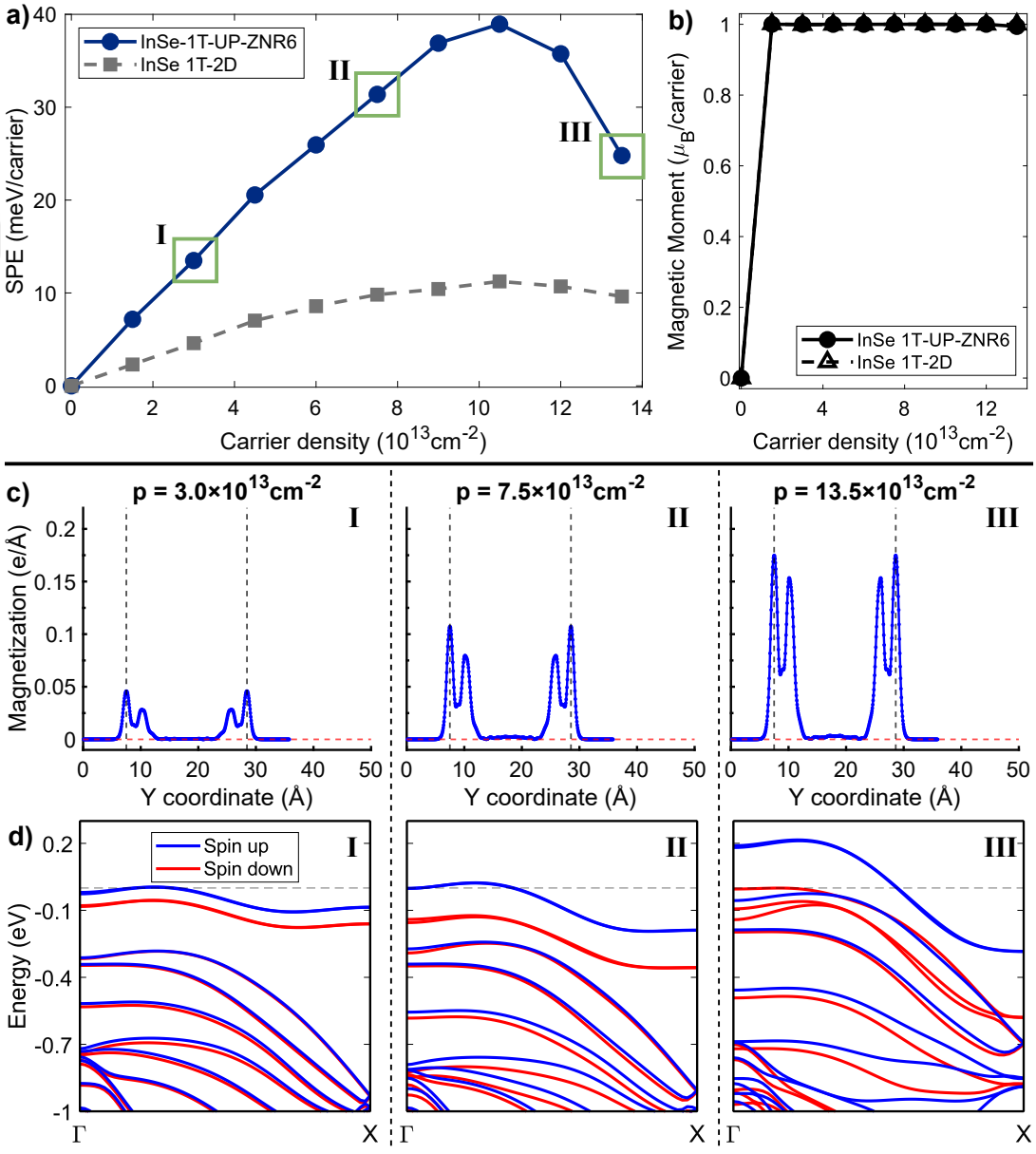

Figure 5.2: InSe 1T-UP-ZNR6 and 1T-2D a) spin polarization energies and b) magnetic moments per carrier as a function of the carrier density. InSe 1T-UP-ZNR6 c) magnetization profiles along the width of NR and d) spin-polarized band structures at different carrier densities.

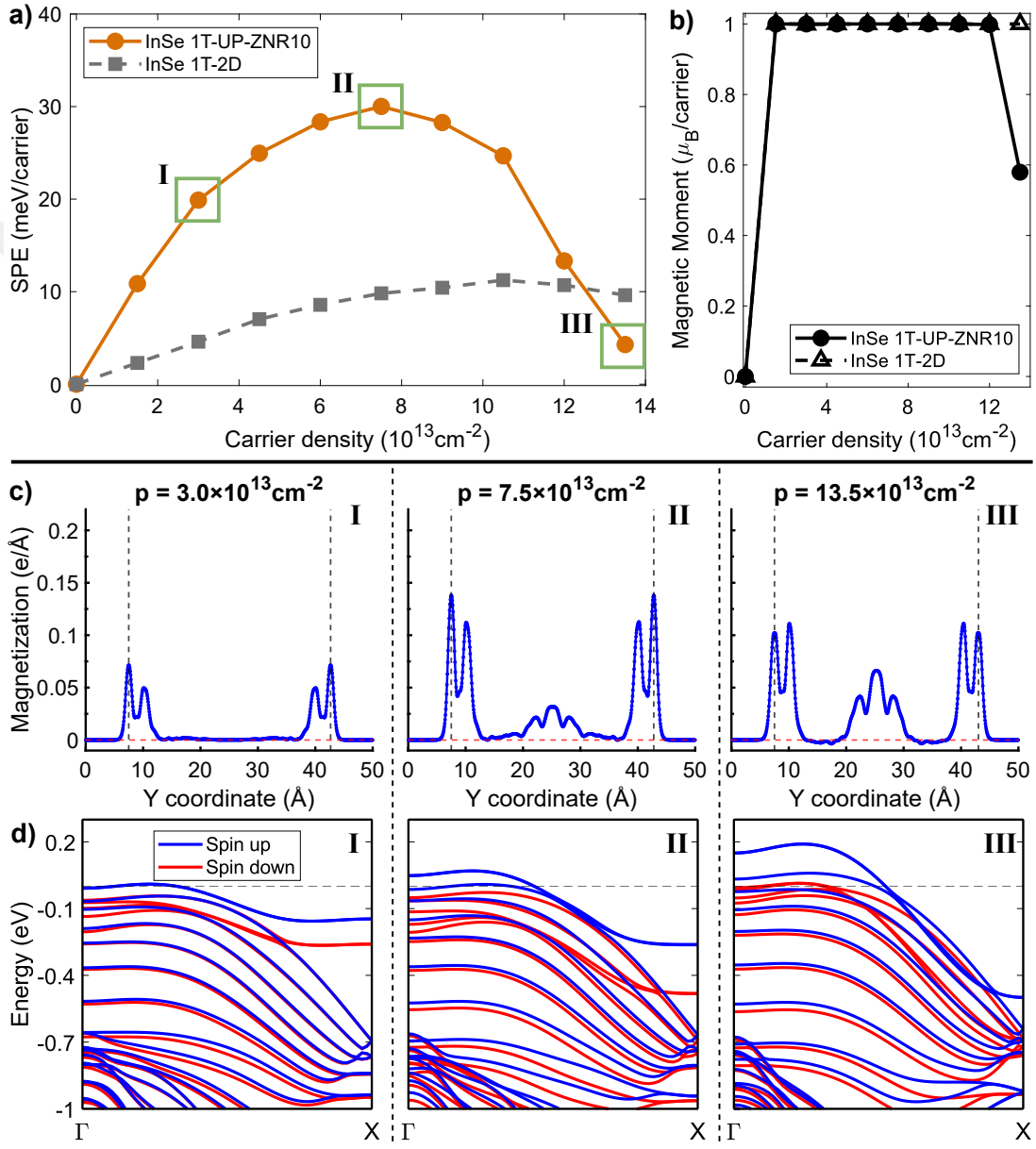

Figure 5.3: InSe 1T-UP-ZNR10 and 1T-2D a) spin polarization energies and b) magnetic moments per carrier as a function of the carrier density. InSe 1T-UP-ZNR10 c) magnetization profiles along the width of NR and d) spin-polarized band structures at different carrier densities.

On the other hand, with increasing NR width and beyond certain doping, carriers also appear in the center region of the NR (see Figure 5.3 (c)). For instance, in the wider InSe 1T-UP-ZNR8, SPE is higher than in InSe 1T-UP-ZNR6 till carriers appear in the center of NR at $p = 9 \times 10^{13}\ cm^{-2}$ (see Figure A.10). Moreover, in the case of even wider NR, InSe 1T-UP-ZNR10, this occurs at even lower doping of $p = 7.5 \times 10^{13}\ cm^{-2}$ as shown in Figure 5.3 (c). This, once again, shows the correlation between edge-localization and SPE. Notably, in the case of InSe 1T-UP-ZNR6, upon hole doping, only the topmost two flat bands cross the E_f (see Figure 5.2 (d)). While in wider InSe 1T-UP-ZNR8 and InSe 1T-UP-ZNR10 (see Figure 5.3), the appearance of carriers in the center region, coincides with the crossing of lower dispersive bulk bands the E_f, in addition to the flat bands. Furthermore, at higher doping densities, the second spin channel also crosses the E_f (see Figures 5.2 (d-III) and 5.3 (d-III)), resulting in a loss of itinerant magnetism, which is particularly noticeable in wider UP-ZNRs (see Figure 5.3 (b)). Consequently, SPE decreases with increasing width, as NRs lose edge-localization, with diminishing confinement effects.

The case of the most narrow InSe 1T-UP-ZNR4 is quite peculiar: the carriers seem to be localized at the edges (see Figure A.12 (c), and SPE shows only an increasing trend across the considered doping range (see Figure A.12 (a)). However, the maximum SPE value is lower than that of wider NRs, which is due to the ratio of edge to the whole ribbon. Despite having localization on the same edge atoms as larger ribbons, these edges are very close to each other and practically near the center of NR. As a result, the magnetic and electronic properties of InSe 1T-UP-ZNR4 differ significantly from those of its wider counterparts. In terms of band structure, we see that with increasing width of InSe 1T-UP-ZNRs, the two valence flat bands become more degenerate, and upon doping, both topmost flat bands cross the E_f (see Figures 5.2 - 5.3). On the other hand, as depicted in Figure A.12 (c) in the case of InSe 1T-UP-ZNR4, these bands are not degenerate, they cross E_f at different carrier densities, and only at $p = 7.5 \times 10^{13}\ cm^{-2}$ the second flat band starts to cross E_f, which can also be observed as a change in its corresponding SPE curve in Figure A.12 (a).

Another prominent example of the correlation between localization and SPE

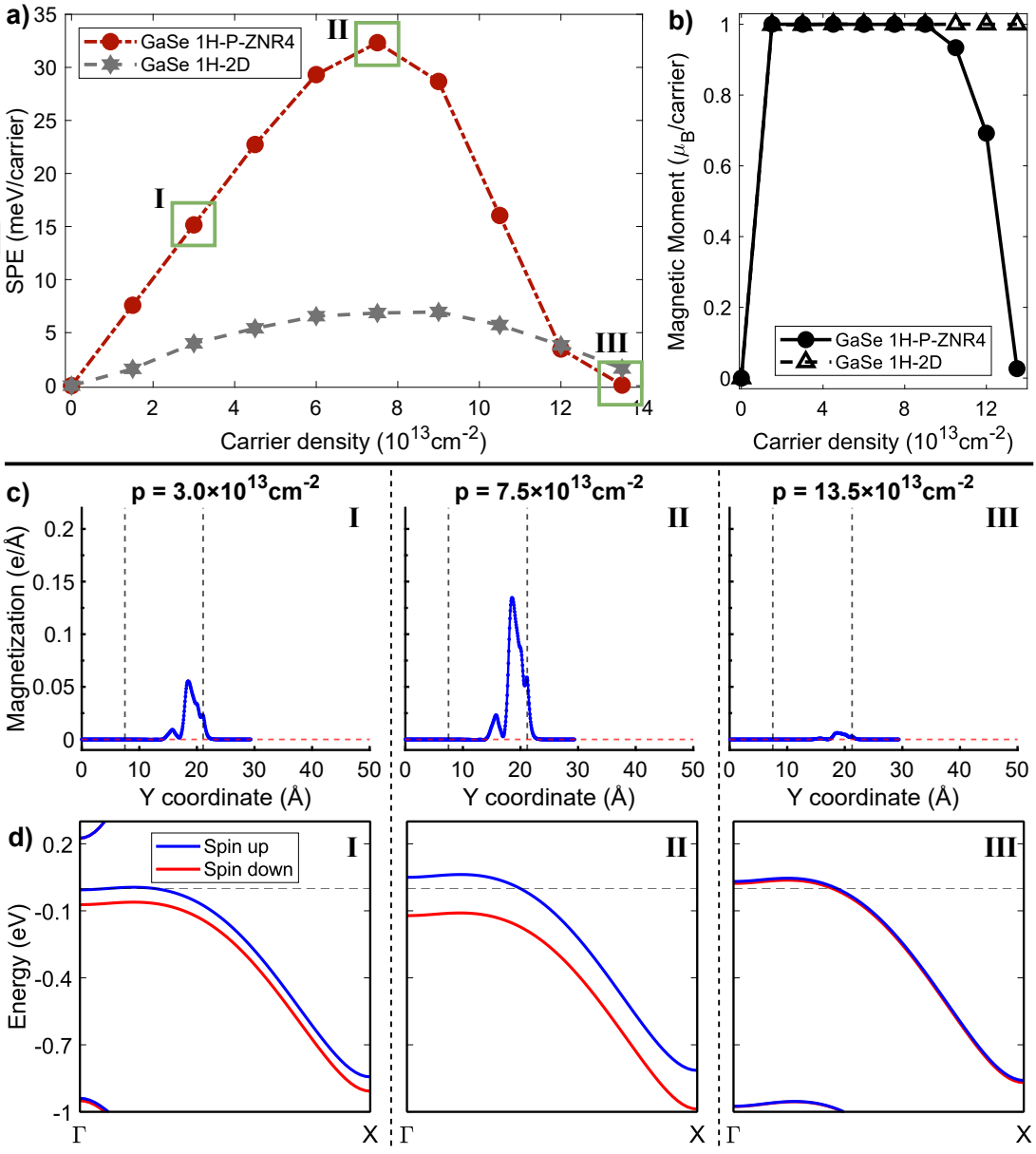

Figure 5.4: GaSe 1H-P-ZNR4 and 1H-2D a) spin polarization energies and b) magnetic moments per carrier as a function of the carrier density. GaSe 1H-P-ZNR4 c) magnetization profiles along the width of NR and d) spin-polarized band structures at different carrier densities.

is the case of GaSe 1H-P-ZNR4. As 1H phase NRs do not possess inversion symmetry and have different atomic coordination on edges (one side only Ga, other only Se atoms), they exhibit outstanding localization only on one edge (see Figure. 5.4 (c)), while previously described 1T-UP-ZNRs exhibit localization on both edges of NRs. Consequently, such a strong edge-localization of 1H-NR, results in SPE as high as 33 meV/carrier at $p = 7.5 \times 10^{13}\ cm^{-2}$ (see Figure. 5.4 (a)), which is about a fivefold increase in SPE compared to its 2D counterpart. However, unlike the aforementioned UP-ZNRs, this system exhibits the topmost valence band with larger bandwidth, meaning less DOS near E_f and quicker loss of itinerant magnetization, as shown in Figure 5.4 (b). Nonetheless, it is important to keep in mind that 1H phase NRs are not thermodynamically favorable, 1T-NRs are.

Notably, a similar correlation between localization and ferromagnetism upon hole doping in low-dimensional materials has been observed in a few recent studies. For instance, Chen et al. [98] investigated hole-doping implications in kagome graphene, which exhibits nearly flat bands topmost valence bands, which originate from single-particle states that localize on hexagonal plaquettes through destructive interference of hopping processes. Consequently, electrons in these states have negligible kinetic energy, and when the flat band is partially filled by hole doping, the overlap of neighboring localized wavefunctions produces a strong exchange interaction, and spontaneous spin splitting is observed. In a related context, our 1T-UP-ZNRs form localized states at the edges of ZNRs, which result in nearly flat distribution in the topmost valence band and, consequently, strong exchange splitting and itinerant ferromagnetism. Furthermore, in a very recent theoretical study [97], the authors demonstrated that chevron GNRs (CGNRs) under an in-plane transverse electric field exhibit collapse of valence and conduction bands into pairs of ultra-flat isolated π-bands. Upon hole-doping, these bands undergo exchange splitting, resulting in half-metallicity. The authors noted that hole distribution in these CGNRs is at protrusions along the edges of the NR, creating a ferromagnetic, one-dimensional spin-1/2 chain along the ribbon length. In addition, Son et al. [99], in their seminal paper on half-metallic ZGNRs, demonstrated how an applied electric field shifts one edge's

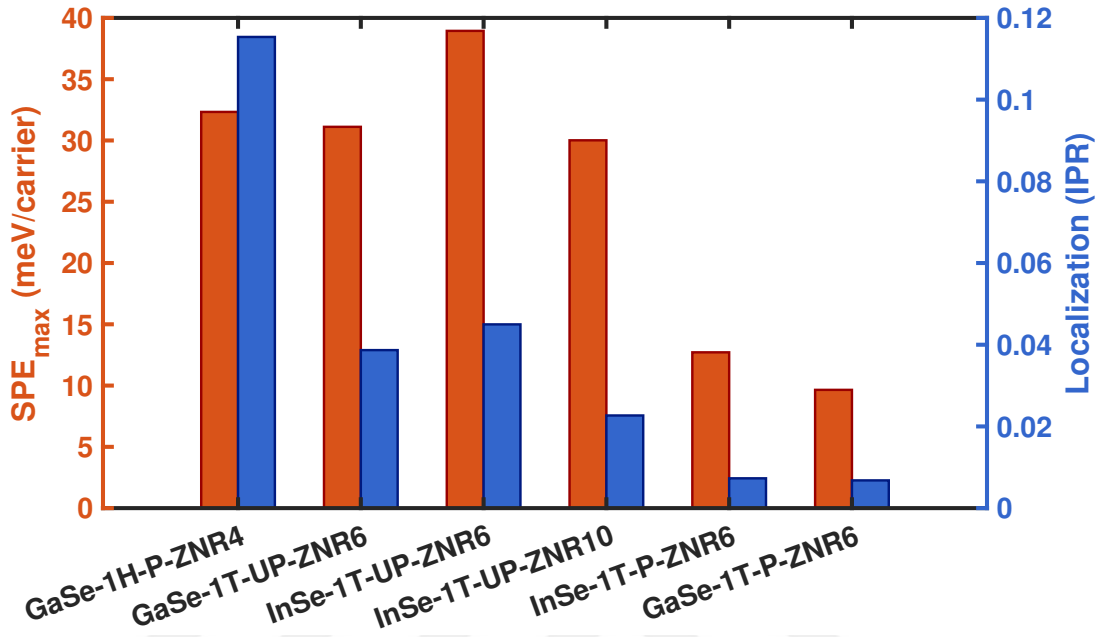

Figure 5.5: Bar plot of the highest spin polarization energies (SPE_{max}, left axis, orange) and localization quantified by inverse participation ratio (IPR, right axis, blue) of magnetization profile at carrier density corresponding to SPE_{max} for selected InSe and GaSe NR structures.

potential down, pulling carriers towards that edge and the other edge's up; such a strong localization limits the kinetic energy, making exchange interactions dominant and resulting in half-metallicity. Remarkably, our GaSe 1H-P-ZNR4 possesses an intrinsic electric field, which results in similar phenomena, exhibiting localization of holes on one edge of the NR and displaying exceptionally high spin-polarization energies and itinerant ferromagnetism.

To quantify and visualize the degree of localization of magnetization (holes) along the width of NRs, we utilize inverse participation ratio (IPR) (see Section 2.8 for more details). In agreement with our discussion above, from Figure 5.5, one can infer that 1H-P-ZNR exhibits the highest localization among considered structures due to its symmetry properties, which cause carriers to accumulate on one end of the NR. The second highest in terms of localization and SPE are 1T-UP-ZNRs; one may note that the degree of localization (IPR values) at the equivalent size of $N = 6$ are practically identical for GaSe and InSe, despite InSe exhibiting higher SPE magnitude. One can also clearly see the consequence

of increasing size and appearance of carriers not only at the edges but also in the center in wider 1T-UP-ZNRs, as shown in the example of InSe 1T-UP-ZNR10, which demonstrates lower IPR value and SPE relative to narrower counterpart. Finally, the 1T-P-ZNRs show significantly lower localization than unpassivated counterparts, regardless of atomic constituents, leading to lower SPE magnitudes. The following section will discuss such NRs with weak edge-localization in more detail.

5.2.2.2 ZNRs with weak edge-localization: 1T-P

1T-P-ZNRs exhibit lower SPE than 1T-UP-ZNRs, as passivation saturates the dangling bonds, eliminating the localized flat band and diminishing edge effects. In both InSe and GaSe configurations, 1T-P-ZNR6s (see Figure 5.6 (a)) demonstrate a maximum SPE value threefold smaller than the corresponding 1T-UP-ZNR6s (see Figure 5.2 (a)). In a related context, the distribution of carriers in 1T-P-ZNRs (see Figures 5.6 (c) and A.14 (c)) is not as localized at the edges as in the case of 1T-UP-ZNRs (see Figures 5.2 (c) and 5.3 (c)), but is more dispersed and closer to the center of NRs. Consequently, the itinerant magnetism in 1T-P-ZNR6 is also observed in the smaller doping range than in the unpassivated counterpart, as shown in Figures 5.6 (b) and 5.2 (b), respectively. Nevertheless, despite 1T-P-ZNRs exhibiting lower SPE than 1T-UP-ZNRs, they still demonstrate higher SPE than 2D counterparts, reaching up to about 30% enhancement at $p = 7.5 \times 10^{13}\ cm^{-2}$.

GaSe 1T-P-ZNR6 and 1T-P-ZNR8 show a similar trend in SPE till $p = 7.5 \times 10^{13}\ cm^{-2}$ (see Figures 5.6 (a) and A.14 (a)), after which 1T-P-ZNR8 displays a significant drop in SPE, as second spin channel also crosses E_f turning it from half metal to normal metal and reducing the magnetization (see Figure A.14). On the other hand, as depicted in Figure 5.6 (b), 1T-P-ZNR6 does not become metallic in the considered doping range, and a reduction in magnetization is observed only from $p = 12 \times 10^{13}\ cm^{-2}$. This behavior indicates that SPE of 1T-P-ZNRs, similar to their unpassivated (UP) counterparts, scales inversely with NR width, which has been previously also observed in hole doped GNRs [60].

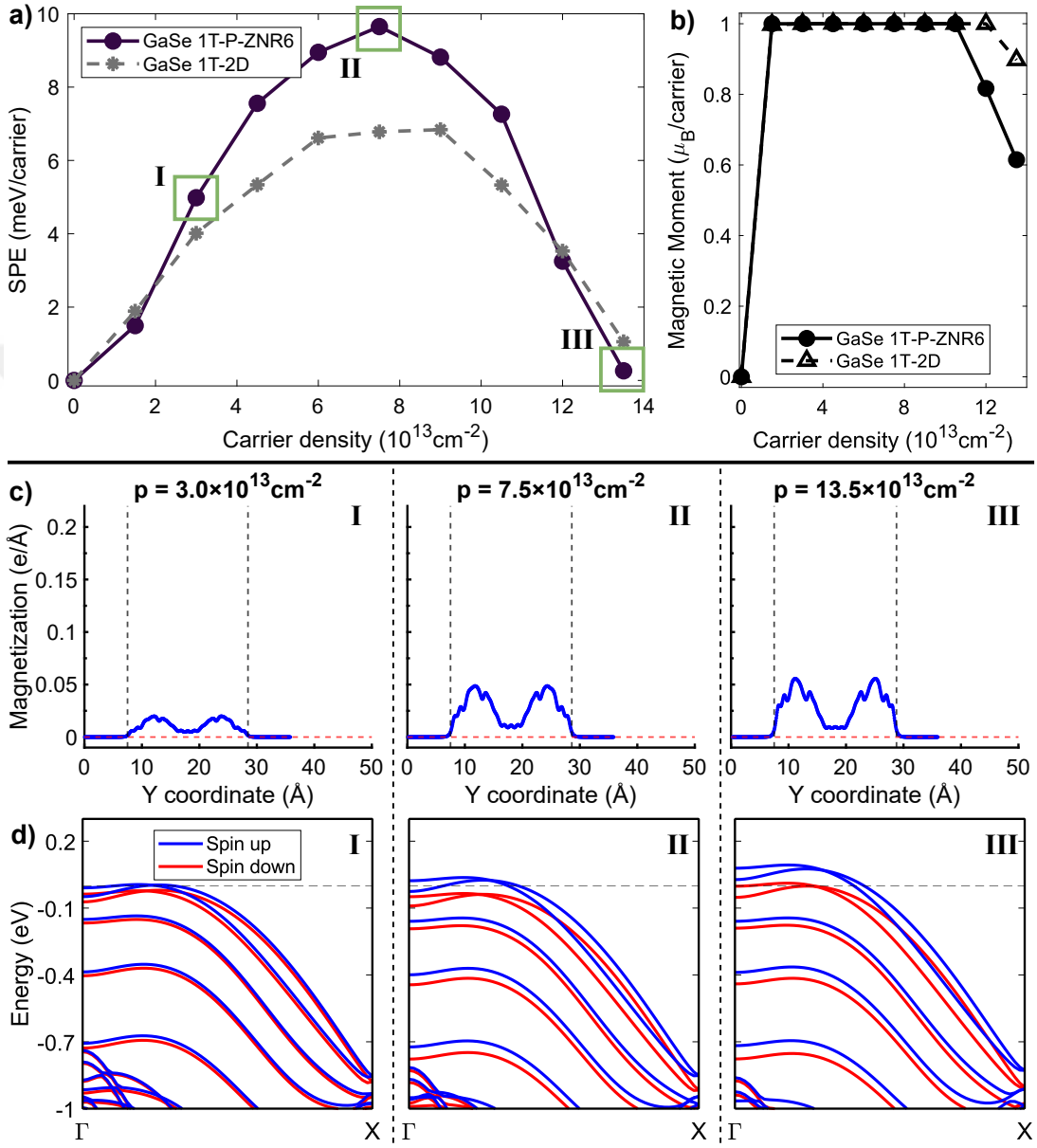

Figure 5.6: GaSe 1T-P-ZNR6 and 1T-2D a) spin polarization energies and b) magnetic moments per carrier as a function of the carrier density. GaSe 1T-P-ZNR6 c) magnetization profiles along the width of NR and d) spin-polarized band structures at different carrier densities.

Nevertheless, despite 1T-P-ZNR4 being narrower, it does not show a higher SPE than 1T-P-ZNR6 or 1T-P-ZNR8 from the same family (see Figure A.13

(a)). As can be seen from the magnetization profiles (Figure A.13 (c)), this ZNR is so narrow that carriers cannot separate to the edges of NR and accumulate in the middle, resulting in lower SPE than in larger widths where carriers are separated and more localized at the edges of NRs. Furthermore, in 1T-P-ZNR4 (see Figure A.13 (d)), only a single band crosses the E_f, while in 1T-P-ZNR6 (see Figure 5.6 (c)) and 1T-P-ZNR8 (Fig. A.14 (c)), two bands cross the E_f.

5.2.3 ANRs

Similar to the previous section, herein, ANRs are examined for comparative analysis and illustration of underlying mechanisms of hole doping. However, once again, it is crucial to note that the structural properties described in Section 2 remain applicable. Particularly, P-ANR(UP-ANR) configurations are thermodynamically less favorable than their P-ZNR(UP-ZNR) counterparts. Nonetheless, we have examined them and present below the most energetically favorable examples, namely InSe 1T-UP-ZNR and GaSe 1H-P-ANR for $N = 6$, to deepen our understanding of the relationships among structure, doping, and magnetic behavior in MX nanoribbons.

Carriers in the InSe 1T-UP-ANR6 in the considered doping range are predominantly localized at the edges (Figure 5.7 (c)). Starting from $p = 10.5 \times 10^{13}\ cm^{-2}$, in addition to edges, magnetization starts to appear near the center of NRs (Figure 5.7 (c)), which coincides with changes in the band structure (see Figure 5.7 (d)), where the second spin-up band cross the E_f , while the spin-down bands start to shift downwards once again (see Figure 5.8), leading to another increasing trend in SPE (see Figure 5.7 (a)). Furthermore, as depicted in Figure 5.7 (c-III), at higher doping rates, flattening of topmost valence bands is observed, associated with increased localization at the edges.

In the case of GaSe 1H-P-ANR6, we observe a maximum SPE of about 10.5 meV/carrier at $p = 6 \times 10^{13}\ cm^{-2}$ (see Figure A.15 (a)). Unlike InSe 1T-UP-ANR, herein, the carriers are dispersed around the center of the NRs (see Figure A.15 (c)). Furthermore,as can be seen from Figure A.15 (d), the topmost valence

band does not exhibit MHS dispersion, and only single band is crossing the E_f upon hole doping. In this context, the spin splitting completely vanishes at high doping rates and consequently SPE also diminishes to zero.

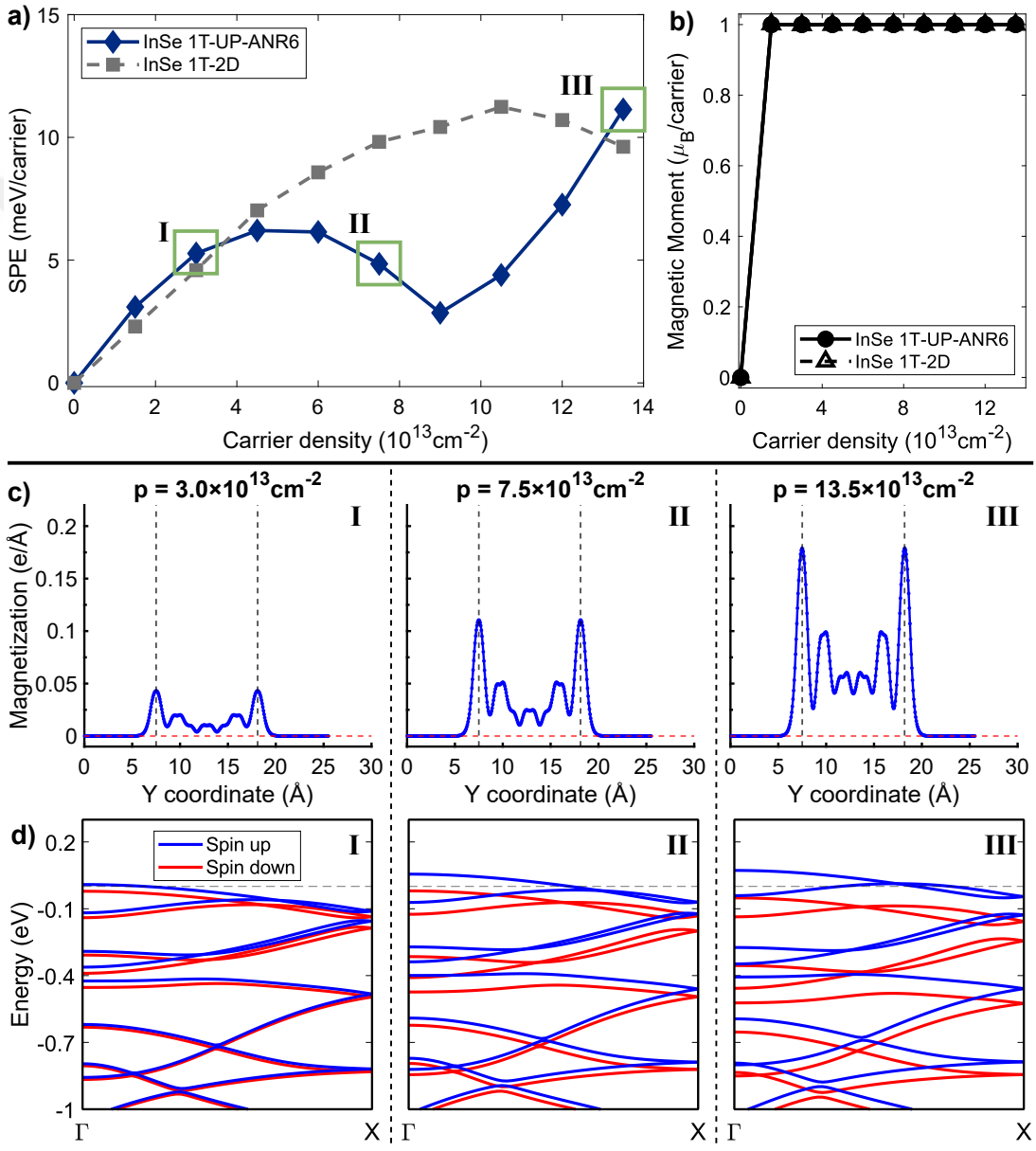

Figure 5.7: InSe 1T-UP-ANR6 and 1T-2D a) spin polarization energies and b) magnetic moments per carrier as a function of the carrier density. InSe 1T-UP-ANR6 c) magnetization profiles along the width of NR and d) spin-polarized band structures at different carrier densities.

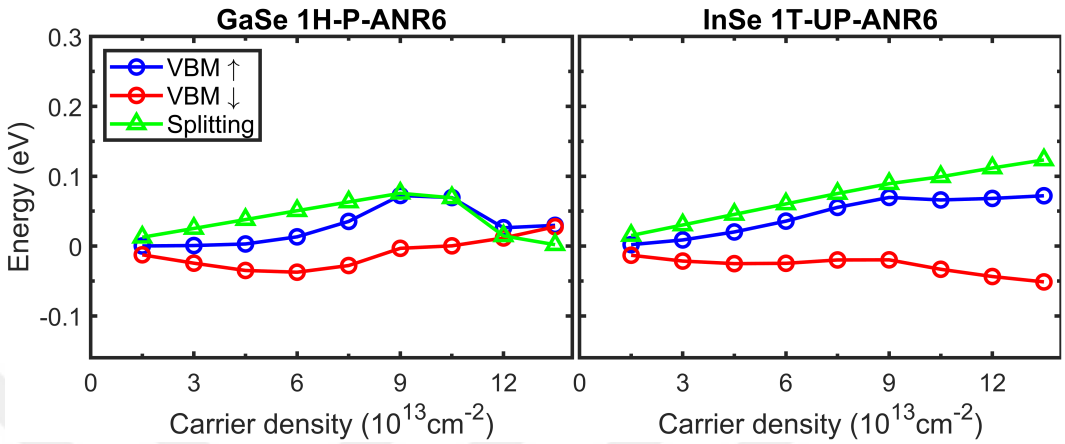

Figure 5.8: ANRs VBM and spin splitting of the topmost valence band vs. carrier density.

5.2.4 Correlation between SPE and VBM trends

Viewed collectively, the results analyzed above reveal a correlation between SPE and valence band maximum (VBM) trends for each spin, which is observed for all MX NRs considered, regardless of atomic constituents, passivation, phase, or edge shape. By comparing the variation of SPE as a function of carrier density with VBM as a function of carrier density in Figures A.16, A.17, and 5.8, one may notice that at carrier densities where SPE exhibits an increasing trend, the spin-up (blue) VBM shifts upwards, while the spin-down (red) VBM shifts downwards; on the contrary, at certain carrier densities where SPE starts to reduce, the spin-down VBM starts to shift upwards. We ascribe this behavior to the progressive shift in the density of states (DOS) with increasing doping. At low doping levels, only the spin-up band moves upward since its top part, characterized by a Mexican-hat profile or a near-flat dispersion, hosts a large DOS (VHS). Once the carrier concentration is high enough that this high-DOS region lies entirely above the E_f, the spin-down band also begins to shift upward, and the SPE then decreases with further doping.

Notably, similar behavior in spin-polarized bands upon hole doping has been reported previously for 2D monolayers of SnS_2 and $SnSe_2$, where one of the

spin-polarized bands was observed to shift upwards, while the one shifted downwards [100]. In addition, Chen et al. reported such behavior not only upon hole doping, but also under tensile and compressive strains in 2D H-MnN_2 monolayer [101]. This phenomenon is attributed to the competition between exchange interactions and kinetic energy in systems exhibiting a sharp singularity near E_f in DOS. In such systems, upon hole doping or strain, the kinetic energy becomes quenched, while the exchange interaction is significantly enhanced, leading to a spontaneous spin splitting of the electronic bands.

Chapter 6

Outlook

In this thesis, we carried out a systematic analysis employing ab initio simulations based on DFT to investigate the width-dependent phase favorability between the 1T and 1H phases of group III metal monochalcogenide (MX, M = Ga, In and X = S, Se) zigzag-edge nanoribbons (ZNRs) and armchair-edge NRs (ANRs), as well as corresponding electrical and magnetic properties in undoped and hole-doped configurations.

Our analysis revealed that, for both hydrogen-passivated ZNRs (P-ZNRs) and unpassivated ZNRs (UP-ZNRs), the nonpolar 1T phase becomes thermodynamically favorable over the polar 1H phase when the ribbon width falls below a critical threshold. This behavior contrasts with the corresponding $2D$ monolayers, in which the 1H polymorph is the thermodynamically stable configuration. The crossover is driven by the competition between the intrinsic electric field and atomic reconstructions, and occurs at widths ranging from 23 nm for GaS up to 34 nm for InSe ZNRs, dimensions that are attainable using contemporary fabrication techniques. In contrast, we discovered that in MX ANRs, the intrinsic electric field is absent in both the 1H and 1T phases. Hence, the difference between formation energies of 1T and 1H phase ANRs is significantly smaller than in ZNRs, and the 1T phase demonstrates thermodynamic favorability over the 1H phase in UP-ANRs exclusively at very narrow widths up to 3.3nm in the

case of InSe. Besides, in P-ANRs, the saturation of edge dangling bonds with hydrogens diminishes the edge effects and makes the 1H phase thermodynamically more favorable even at minimal NR widths. Furthermore, unlike GaS and GaSe NRs, in the case of InSe NRs, both ZNRs and ANRs show positive hydrogenation energies, indicating that UP-NRs are more thermodynamically favorable than P-NRs.

Notably, the intrinsic built-in potential in 1H ZNRs significantly influences not only their structural characteristics but also their electronic properties. Our results reveal that polar MX 1H ZNRs remain metallic even after hydrogen passivation, whereas nonpolar MX 1T ZNRs preserve a finite band gap independent of both passivation and ribbon width. In addition, for MX 1T-P-ZNRs, the highest valence band continues to exhibit a Mexican-hat dispersion similar to that of the corresponding 2D monolayers, and the magnitude of the band gap monotonically decreases toward the monolayer value. These characteristics make these NRs attractive for thermoelectric and optoelectronic device applications. Moreover, the positive hydrogenation energies, together with the nearly flat valence-band maxima, suggest that InSe 1T-UP-ZNRs are promising candidates for spintronic applications. On the other hand, all MX ANRs are nonmagnetic semiconductors without the MHS dispersion in the topmost valence band. The band gaps of MX 1T ANRs exhibit an oscillatory behavior as a function of ribbon width N, alternating between even and odd N, and this oscillation amplitude diminishes as N increases. Similar to zigzag-edge counterparts, 1T-P-ANR band gaps also exhibit a downward trend asymptotically approaching 2D monolayer values with increasing width. These findings demonstrate that the electronic and magnetic properties of MX NRs are strongly governed by their dimensionality and edge configuration. Systematic modulation of bandgap, magnetic ordering, and charge-carrier characteristics can be achieved through tailored selection of crystallographic phase (1H or 1T), edge termination (zigzag or armchair), and edge passivation. This establishes a rational framework for the design of MX NRs in nanoelectronics and spintronics.

Consequently, we systematically investigated how the magnetic properties alter upon hole doping in these MX NRs, examining the interplay between reduced

dimensionality, electronic structure modulation, and spin distributions that are distinct from their 2D counterparts. We considered hole doping of MX NRs of 1T and 1H phases, with both zigzag and armchair edges, as well as with and without hydrogen passivation. The stability of the ferromagnetic state was evaluated via spin-polarization energies (SPEs) by comparing both magnetization density profiles and the corresponding electronic band structures of the investigated architectures. We discovered that upon hole doping, NRs exhibit itinerant magnetization and half-metallicity in a broad doping range, as well as SPE magnitudes significantly higher than in their 2D counterparts. The primary cause of this enhancement lies in the edge-localization of carriers in hole-doped MX NRs as a result of the quantum confinement effect. Higher edge-localization results in sharper singularity near the Fermi level in DOS and, subsequently, higher SPE. To quantify the degree of localization of holes along the width of NRs depicted in magnetization profile plots, we utilized the inverse participation ratio (IPR). We showed that 1H-P-ZNR exhibits the highest localization among considered structures due to its symmetry properties with distinct atomic environments at the edges, which causes all carriers to accumulate on one end of the NR, limiting the kinetic energy, hence making exchange interactions dominant and resulting in half-metallicity. The second highest in terms of localization and SPE are 1T-UP-ZNRs, which also show strong edge localization, independent of atomic composition, but on both edges, due to the inversion symmetry of the 1T phase. Nonetheless, with increasing width of these 1T-UP-ZNRs, we observed the appearance of carriers not only at the edges but also in the center of wider 1T-UP-ZNRs, as shown in the example of InSe 1T-UP-ZNR10, which demonstrates lower IPR value and SPE relative to narrower counterpart. Finally, the 1T-P-ZNRs show significantly lower localization than their unpassivated counterparts, regardless of atomic constituents, leading to lower SPE magnitudes.

The findings in this thesis pave the way for a range of future research directions, including the investigation of width-dependent phase transition in NRs of other material families that exhibit polymorphism in 2D. Such studies could reveal a variety of electronic and magnetic phase changes analogous to those reported in this work, and might ultimately enable novel practical applications.

Ultimately, the 1D confinement of 2D structures can be extended to other materials exhibiting Mexican-hat–shaped dispersions in the topmost valence band, potentially enhancing ferromagnetic stability upon hole-doping even at low carrier concentrations.

Bibliography

[1] E. Aliyev, A. Mobaraki, H. Sevinçli, and S. Jahangirov, "Thermodynamic favorability of the 1T phase over the 1H phase in group III metal monochalcogenide zigzag nanoribbons," *The Journal of Physical Chemistry C*, vol. 129, no. 17, pp. 8354–8360, 2025.

[2] M. T. Lusk and A. E. Mattsson, "High-performance computing for materials design to advance energy science," *MRS Bulletin*, vol. 36, no. 3, pp. 169–174, 2011.

[3] T. Cao, Z. Li, and S. G. Louie, "Tunable magnetism and half-metallicity in hole-doped monolayer gase," *Physical review letters*, vol. 114, no. 23, p. 236602, 2015.

[4] A. K. Geim and K. S. Novoselov, "The rise of graphene," *Nature materials*, vol. 6, no. 3, pp. 183–191, 2007.

[5] L. Jiao, L. Zhang, X. Wang, G. Diankov, and H. Dai, "Narrow graphene nanoribbons from carbon nanotubes," *Nature*, vol. 458, no. 7240, pp. 877–880, 2009.

[6] Z. Chen, Y.-M. Lin, M. J. Rooks, and P. Avouris, "Graphene nano-ribbon electronics," *Physica E: Low-dimensional Systems and Nanostructures*, vol. 40, no. 2, pp. 228–232, 2007.

[7] J. Cai, P. Ruffieux, R. Jaafar, M. Bieri, T. Braun, S. Blankenburg, M. Muoth, A. P. Seitsonen, M. Saleh, X. Feng, *et al.*, "Atomically precise bottom-up fabrication of graphene nanoribbons," *Nature*, vol. 466, no. 7305, pp. 470–473, 2010.

[8] Y. Chen, P. Cui, X. Ren, C. Zhang, C. Jin, Z. Zhang, and C.-K. Shih, "Fabrication of MoSe2 nanoribbons via an unusual morphological phase transition," *Nature communications*, vol. 8, no. 1, p. 15135, 2017.

[9] Y.-W. Son, M. L. Cohen, and S. G. Louie, "Energy gaps in graphene nanoribbons," *Physical review letters*, vol. 97, no. 21, p. 216803, 2006.

[10] A. Bellunato, H. Arjmandi Tash, Y. Cesa, and G. F. Schneider, "Chemistry at the Edge of Graphene," *ChemPhysChem*, vol. 17, no. 6, pp. 785–801, 2016.

[11] L. Talirz, H. Söde, J. Cai, P. Ruffieux, S. Blankenburg, R. Jafaar, R. Berger, X. Feng, K. Müllen, D. Passerone, *et al.*, "Termini of bottom-up fabricated graphene nanoribbons," *Journal of the American Chemical Society*, vol. 135, no. 6, pp. 2060–2063, 2013.

[12] Z. Wang, D. Fan, M. Yin, H. Li, H. Hu, F. Guo, Z. Feng, J. Li, D. Zhang, Z. Li, *et al.*, "Potential applications of C 2 N-h2D/BN nanoribbon adsorption of transition metals in spintronic devices and magnetic storage devices," *New Journal of Chemistry*, vol. 48, no. 11, pp. 4699–4707, 2024.

[13] S. Kumar, S. Pratap, V. Kumar, R. K. Mishra, J. S. Gwag, and B. Chakraborty, "Electronic, transport, magnetic, and optical properties of graphene nanoribbons and their optical sensing applications: A comprehensive review," *Luminescence*, vol. 38, no. 7, pp. 909–953, 2023.

[14] Z. He, K. Wang, C. Yan, L. Wan, Q. Zhou, T. Zhang, X. Ye, Y. Zhang, F. Shi, S. Jiang, *et al.*, "Controlled preparation and device application of sub-5 nm graphene nanoribbons and graphene nanoribbon/carbon nanotube intramolecular heterostructures," *ACS Applied Materials & Interfaces*, vol. 15, no. 5, pp. 7148–7156, 2023.

[15] M. Aparna and R. Chatanathodi, "Oxygen reduction and hydrogen evolution reactions on zigzag ReS2 nanoribbons," *Applied Surface Science*, vol. 618, p. 156677, 2023.

[16] H. Hou, L. Cardo, J. Merino, F. Xu, C. Wetzl, B. Arnaiz, X. Luan, Y. Mai, A. Criado, and M. Prato, "PEGylated bottom-up synthesized graphene nanoribbons loaded with camptothecin as potential drug carriers," *Materials Today Chemistry*, vol. 33, p. 101668, 2023.

[17] S. Dutta and S. K. Pati, "Novel properties of graphene nanoribbons: a review," *Journal of Materials Chemistry*, vol. 20, no. 38, pp. 8207–8223, 2010.

[18] Y. C. Lin, Z. Mutlu, G. B. Barin, Y. Hong, J. P. Llinas, A. Narita, H. Singh, K. Müllen, P. Ruffieux, R. Fasel, *et al.*, "Scaling and statistics of bottom-up synthesized armchair graphene nanoribbon transistors," *Carbon*, vol. 205, pp. 519–526, 2023.

[19] J. P. Llinas, A. Fairbrother, G. Borin Barin, W. Shi, K. Lee, S. Wu, B. Yong Choi, R. Braganza, J. Lear, N. Kau, *et al.*, "Short-channel field-effect transistors with 9-atom and 13-atom wide graphene nanoribbons," *Nature communications*, vol. 8, no. 1, p. 633, 2017.

[20] P. B. Bennett, Z. Pedramrazi, A. Madani, Y.-C. Chen, D. G. de Oteyza, C. Chen, F. R. Fischer, M. F. Crommie, and J. Bokor, "Bottom-up graphene nanoribbon field-effect transistors," *Applied Physics Letters*, vol. 103, no. 25, 2013.

[21] G. Lee and K. Cho, "Electronic structures of zigzag graphene nanoribbons with edge hydrogenation and oxidation," *Physical Review B—Condensed Matter and Materials Physics*, vol. 79, no. 16, p. 165440, 2009.

[22] M. Yagmurcukardes, F. M. Peeters, R. T. Senger, and H. Sahin, "Nanoribbons: From fundamentals to state-of-the-art applications," *Applied Physics Reviews*, vol. 3, no. 4, 2016.

[23] M. Yu, S. A. Iddawela, J. Wang, M. Hilse, J. L. Thompson, D. Reifsnyder Hickey, S. B. Sinnott, and S. Law, "Quasi-Van der Waals Epitaxial Growth of γ'-GaSe Nanometer-Thick Films on GaAs (111) B Substrates," *ACS nano*, vol. 18, no. 26, pp. 17185–17196, 2024.

[24] Y. Gutiérrez, F. Agresti, D. Juan, S. Dicorato, M. M. Giangregorio, F. Moreno, P. García-Fernández, J. Junquera, L. Armelao, and M. Losurdo, "Unveiling Polymorphs and Polytypes of the 2D Layered Semiconducting Gallium Monosulfide," *Advanced Optical Materials*, vol. 12, no. 15, p. 2303002, 2024.

[25] W. Li, X. Zhang, J. Yang, S. Zhou, C. Song, P. Cheng, Y.-Q. Zhang, B. Feng, Z. Wang, Y. Lu, *et al.*, "Emergence of ferroelectricity in a non-ferroelectric monolayer," *Nature Communications*, vol. 14, no. 1, p. 2757, 2023.

[26] T. Hu, C. Xu, A. Zhang, and P. Yu, "Prediction of new phase 2D C 2h group III monochalcogenides with direct bandgaps and highly anisotropic carrier mobilities," *Materials Advances*, vol. 3, no. 4, pp. 2213–2221, 2022.

[27] C. Wen, Z. Zhang, Z. Guo, J. Shen, B. Sa, P. Lin, J. Zhou, and Z. Sun, "Two-dimensional O-phase group III monochalcogenides for photocatalytic water splitting," *Journal of Physics: Condensed Matter*, vol. 32, no. 6, p. 065501, 2019.

[28] H. Bergeron, D. Lebedev, and M. C. Hersam, "Polymorphism in post-dichalcogenide two-dimensional materials," *Chemical Reviews*, vol. 121, no. 4, pp. 2713–2775, 2021.

[29] J. Grzonka, M. S. Claro, A. Molina-Sánchez, S. Sadewasser, and P. J. Ferreira, "Novel polymorph of GaSe," *Advanced Functional Materials*, vol. 31, no. 48, p. 2104965, 2021.

[30] X. Li, L. Li, and M. Wu, "Various polymorphs of group III–VI (GaSe, InSe, GaTe) monolayers with quasi-degenerate energies: Facile phase transformations, high-strain plastic deformation, and ferroelastic switching," *Materials Today Physics*, vol. 15, p. 100229, 2020.

[31] J. Zhou and H. L. Zhuang, "First-Principles Study on the 1T Phase of GaX (X= S, Se) Monolayers," *ChemistrySelect*, vol. 1, no. 18, pp. 5779–5783, 2016.

[32] H. Nitta, T. Yonezawa, A. Fleurence, Y. Yamada-Takamura, and T. Ozaki, "First-principles study on the stability and electronic structure of monolayer GaSe with trigonal-antiprismatic structure," *Physical Review B*, vol. 102, no. 23, p. 235407, 2020.

[33] Z. Yang and J. Hao, "Recent progress in 2d layered III–VI semiconductors and their heterostructures for optoelectronic device applications," *Advanced Materials Technologies*, vol. 4, no. 8, p. 1900108, 2019.

[34] M. Yu, M. Hilse, Q. Zhang, Y. Liu, Z. Wang, and S. Law, "Review of Nanolayered Post-transition Metal Monochalcogenides: Synthesis, Properties, and Applications," *ACS Applied Nano Materials*, vol. 7, no. 24, pp. 28008–28026, 2024.

[35] D. A. Bandurin, A. V. Tyurnina, G. L. Yu, A. Mishchenko, V. Zólyomi, S. V. Morozov, R. K. Kumar, R. V. Gorbachev, Z. R. Kudrynskyi, S. Pezzini, *et al.*, "High electron mobility, quantum hall effect and anomalous optical response in atomically thin InSe," *Nature nanotechnology*, vol. 12, no. 3, pp. 223–227, 2017.

[36] M. Brotons-Gisbert, D. Andres-Penares, J. Suh, F. Hidalgo, R. Abargues, P. J. Rodriguez-Canto, A. Segura, A. Cros, G. Tobias, E. Canadell, *et al.*, "Nanotexturing to enhance photoluminescent response of atomically thin indium selenide with highly tunable band gap," *Nano letters*, vol. 16, no. 5, pp. 3221–3229, 2016.

[37] J. Jiang, L. Xu, C. Qiu, and L.-M. Peng, "Ballistic two-dimensional InSe transistors," *Nature*, vol. 616, no. 7957, pp. 470–475, 2023.

[38] Y. Xiong, D. Xu, Y. Feng, G. Zhang, P. Lin, and X. Chen, "P-Type 2D Semiconductors for Future Electronics," *Advanced Materials*, vol. 35, no. 50, p. 2206939, 2023.

[39] P. Sutter, J. S. French, L. Khosravi Khorashad, C. Argyropoulos, and E. Sutter, "Optoelectronics and nanophotonics of vapor–liquid–solid grown GaSe van der Waals nanoribbons," *Nano letters*, vol. 21, no. 10, pp. 4335–4342, 2021.

[40] P. Hauchecorne, F. Gity, M. Martin, H. Okuno, S. Bhattacharjee, J. Moeyaert, D. Rouchon, B. Hyot, P. K. Hurley, and T. Baron, "Gallium selenide nanoribbons on silicon substrates for photodetection," *ACS Applied Nano Materials*, vol. 4, no. 8, pp. 7820–7831, 2021.

[41] E. Sutter, J. S. French, S. Sutter, J. C. Idrobo, and P. Sutter, "Vapor–liquid–solid growth and optoelectronics of gallium sulfide van der Waals nanowires," *ACS nano*, vol. 14, no. 5, pp. 6117–6126, 2020.

[42] C.-Y. Wu, H. Zhu, M. Wang, J. Kang, C. Xie, L. Wang, and L.-B. Luo, "Controlled synthesis of GaSe microbelts for high-gain photodetectors induced by the electron trapping effect," *Journal of Materials Chemistry C*, vol. 8, no. 16, pp. 5375–5379, 2020.

[43] X. Xiong, Q. Zhang, X. Zhou, B. Jin, H. Li, and T. Zhai, "One-step synthesis of p-type GaSe nanoribbons and their excellent performance in photodetectors and phototransistors," *Journal of Materials Chemistry C*, vol. 4, no. 33, pp. 7817–7823, 2016.

[44] G. Shen, D. Chen, P.-C. Chen, and C. Zhou, "Vapor- solid growth of one-dimensional layer-structured gallium sulfide nanostructures," *Acs Nano*, vol. 3, no. 5, pp. 1115–1120, 2009.

[45] S. K. Panda, A. Datta, G. Sinha, S. Chaudhuri, P. G. Chavan, S. S. Patil, M. A. More, and D. S. Joag, "Synthesis of well-crystalline GaS nanobelts and their unique field emission behavior," *The Journal of Physical Chemistry C*, vol. 112, no. 16, pp. 6240–6244, 2008.

[46] H. Arora and A. Erbe, "Recent progress in contact, mobility, and encapsulation engineering of InSe and GaSe," *InfoMat*, vol. 3, no. 6, pp. 662–693, 2021.

[47] B.-J. Wang, X.-H. Li, L.-W. Zhang, G.-D. Wang, and S.-H. Ke, "Electronic structures and edge effects of Ga2S2 nanoribbons," *Chinese Physics B*, vol. 25, no. 10, p. 107101, 2016.

[48] Y. Zhou, S. Li, W. Zhou, X. Zu, and F. Gao, "Evidencing the existence of intrinsic half-metallicity and ferromagnetism in zigzag gallium sulfide nanoribbons," *Scientific reports*, vol. 4, no. 1, p. 5773, 2014.

[49] M. Mosaferi, I. A. Sarsari, and M. Alaei, "Band structure engineering in gallium sulfide nanostructures," *Applied Physics A*, vol. 127, no. 2, p. 123, 2021.

[50] M. Wu, J.-j. Shi, M. Zhang, Y.-m. Ding, H. Wang, Y.-l. Cen, W.-h. Guo, S.-h. Pan, and Y.-h. Zhu, "Modulation of electronic and magnetic properties in InSe nanoribbons: edge effect," *Nanotechnology*, vol. 29, no. 20, p. 205708, 2018.

[51] X. Cheng, C. Zhang, L. Guan, and J. Tao, "Origin of high hydrogen evolution activity on InSe nanoribbons: A first-principles study," *International Journal of Hydrogen Energy*, vol. 44, no. 44, pp. 24174–24183, 2019.

[52] L. Kou, C. Tang, Y. Zhang, T. Heine, C. Chen, and T. Frauenheim, "Tuning magnetism and electronic phase transitions by strain and electric field in zigzag mos2 nanoribbons," *The journal of physical chemistry letters*, vol. 3, no. 20, pp. 2934–2941, 2012.

[53] E. Taghizadeh Sisakht, F. Fazileh, M. Zare, M. Zarenia, and F. Peeters, "Strain-induced topological phase transition in phosphorene and in phosphorene nanoribbons," *Physical Review B*, vol. 94, no. 8, p. 085417, 2016.

[54] F. Güller, A. M. Llois, J. Goniakowski, and C. Noguera, "Prediction of structural and metal-to-semiconductor phase transitions in nanoscale MoS 2, WS 2, and other transition metal dichalcogenide zigzag ribbons," *Physical Review B*, vol. 91, no. 7, p. 075407, 2015.

[55] P. Hohenberg and W. Kohn, "Inhomogeneous electron gas," *Physical review*, vol. 136, no. 3B, p. B864, 1964.

[56] W. Kohn and L. J. Sham, "Self-consistent equations including exchange and correlation effects," *Physical review*, vol. 140, no. 4A, p. A1133, 1965.

[57] B.-J. Wang, X.-H. Li, L.-W. Zhang, G.-D. Wang, and S.-H. Ke, "Strain engineering of electronic and magnetic properties of Ga2S2 nanoribbons," *Chinese Physics B*, vol. 26, no. 5, p. 057102, 2017.

[58] J. Zhou, "Structures and electronic properties of GaSe and GaS nanoribbons," *RSC advances*, vol. 5, no. 115, pp. 94679–94684, 2015.

[59] K. Iordanidou, M. Houssa, J. Kioseoglou, V. Afanas' ev, A. Stesmans, and C. Persson, "Hole-doped 2d inse for spintronic applications," *ACS Applied Nano Materials*, vol. 1, no. 12, pp. 6656–6665, 2018.

[60] S. Gao and L. Yang, "Edge-insensitive magnetism and half metallicity in graphene nanoribbons," *Journal of Physics: Condensed Matter*, vol. 30, no. 48, p. 48LT01, 2018.

[61] D. M. Ceperley and B. J. Alder, "Ground state of the electron gas by a stochastic method," *Physical review letters*, vol. 45, no. 7, p. 566, 1980.

[62] J. P. Perdew and Y. Wang, "Accurate and simple analytic representation of the electron-gas correlation energy," *Physical review B*, vol. 45, no. 23, p. 13244, 1992.

[63] J. P. Perdew, K. Burke, and M. Ernzerhof, "Generalized gradient approximation made simple," *Physical review letters*, vol. 77, no. 18, p. 3865, 1996.

[64] A. V. Krukau, O. A. Vydrov, A. F. Izmaylov, and G. E. Scuseria, "Influence of the exchange screening parameter on the performance of screened hybrid functionals," *The Journal of chemical physics*, vol. 125, no. 22, 2006.

[65] D. Vanderbilt, "Soft self-consistent pseudopotentials in a generalized eigenvalue formalism," *Physical review B*, vol. 41, no. 11, p. 7892, 1990.

[66] P. E. Blöchl, "Projector augmented-wave method," *Physical review B*, vol. 50, no. 24, p. 17953, 1994.

[67] G. Kresse and J. Furthmüller, "Efficient iterative schemes for ab initio total-energy calculations using a plane-wave basis set," *Physical review B*, vol. 54, no. 16, p. 11169, 1996.

[68] R. Bell and P. Dean, "Atomic vibrations in vitreous silica," *Discussions of the Faraday society*, vol. 50, pp. 55–61, 1970.

[69] M. Jaiswal, C. H. Yi Xuan Lim, Q. Bao, C. T. Toh, K. P. Loh, and B. Ozyilmaz, "Controlled hydrogenation of graphene sheets and nanoribbons," *ACS nano*, vol. 5, no. 2, pp. 888–896, 2011.

[70] M. Pan, E. C. Girao, X. Jia, S. Bhaviripudi, Q. Li, J. Kong, V. Meunier, and M. S. Dresselhaus, "Topographic and spectroscopic characterization of electronic edge states in cvd grown graphene nanoribbons," *Nano letters*, vol. 12, no. 4, pp. 1928–1933, 2012.

[71] Z. Deng, D. Cao, J. He, S. Lin, S. M. Lindsay, and Y. Liu, "Solution synthesis of ultrathin single-crystalline sns nanoribbons for photodetectors via phase transition and surface processing," *ACS nano*, vol. 6, no. 7, pp. 6197–6207, 2012.

[72] P. Z. Hanakata, S. S. Bhabesh, D. Yllanes, D. R. Nelson, and M. J. Bowick, "Vibrations and transitions across barrier of strained nanoribbons at finite temperature," *Physical Review Materials*, vol. 8, no. 1, p. 016001, 2024.

[73] H. Cai, Y. Gu, Y.-C. Lin, Y. Yu, D. B. Geohegan, and K. Xiao, "Synthesis and emerging properties of 2D layered III–VI metal chalcogenides," *Applied Physics Reviews*, vol. 6, no. 4, 2019.

[74] M. N. Çınar, G. Ö. Sargın, K. Sevim, B. Özdamar, G. Kurt, and H. Sevinçli, "Ballistic thermoelectric transport properties of two-dimensional group III-VI monolayers," *Physical Review B*, vol. 103, no. 16, p. 165422, 2021.

[75] G. Kresse and D. Joubert, "From ultrasoft pseudopotentials to the projector augmented-wave method," *Physical review B*, vol. 59, no. 3, p. 1758, 1999.

[76] G. Kresse and J. Hafner, "Ab initio molecular dynamics for liquid metals," *Physical review B*, vol. 47, no. 1, p. 558, 1993.

[77] G. Kresse and J. Furthmüller, "Efficiency of ab-initio total energy calculations for metals and semiconductors using a plane-wave basis set," *Computational materials science*, vol. 6, no. 1, pp. 15–50, 1996.

[78] V. Zólyomi, N. Drummond, and V. Fal'ko, "Electrons and phonons in single layers of hexagonal indium chalcogenides from ab initio calculations," *Physical Review B*, vol. 89, no. 20, p. 205416, 2014.

[79] M. A. Aslam, T. H. Tran, A. Supina, O. Siri, V. Meunier, K. Watanabe, T. Taniguchi, M. Kralj, C. Teichert, E. Sheremet, *et al.*, "Single-crystalline nanoribbon network field effect transistors from arbitrary two-dimensional materials," *npj 2D Materials and Applications*, vol. 6, no. 1, p. 76, 2022.

[80] W. Zan, Z. Zhang, Y. Yang, X. Yao, S. Li, and B. I. Yakobson, "Width-dependent phase crossover in transition metal dichalcogenide nanoribbons," *Nanotechnology*, vol. 30, no. 7, p. 075701, 2018.

[81] J.-H. Song, T. Akiyama, and A. J. Freeman, "Stabilizing mechanism of the dipolar structure and its effects on formation of carriers in wurtzite {0001} films: InN and ZnO," *Physical Review B—Condensed Matter and Materials Physics*, vol. 77, no. 3, p. 035332, 2008.

[82] J. Li, J. Gayles, N. Kioussis, Z. Zhang, C. Grein, and F. Aqariden, "Ab initio studies of the unreconstructed polar CdTe (111) surface," *Journal of electronic materials*, vol. 41, no. 10, pp. 2745–2753, 2012.

[83] A. Yamanaka and S. Okada, "Polarity control of h-BN nanoribbon edges by strain and edge termination," *Physical Chemistry Chemical Physics*, vol. 19, no. 13, pp. 9113–9117, 2017.

[84] Z. Zhong, G. Koster, and P. J. Kelly, "Prediction of thickness limits of ideal polar ultrathin films," *Physical Review B*, vol. 85, no. 12, p. 121411, 2012.

[85] B. Kuiper, D. Samal, D. H. Blank, J. E. ten Elshof, G. Rijnders, and G. Koster, "Control of oxygen sublattice structure in ultra-thin srcuo2 films studied by x-ray photoelectron diffraction," *APL materials*, vol. 1, no. 4, p. 042113, 2013.

[86] A.-L. Yao, X.-F. Wang, Y.-S. Liu, and Y.-N. Sun, "Electronic structure and i-v characteristics of inse nanoribbons," *Nanoscale Research Letters*, vol. 13, pp. 1–7, 2018.

[87] J. Paier, M. Marsman, K. Hummer, G. Kresse, I. C. Gerber, and J. G. Ángyán, "Screened hybrid density functionals applied to solids," *The Journal of chemical physics*, vol. 124, no. 15, p. 154709, 2006.

[88] C.-H. Park and S. G. Louie, "Energy gaps and stark effect in boron nitride nanoribbons," *Nano letters*, vol. 8, no. 8, pp. 2200–2203, 2008.

[89] M. Filatov, A. Pomogaeva, and S. K. Min, "Implications of the edge states for the band structure of armchair graphene nanoribbons," *Carbon Letters*, pp. 1–13, 2024.

[90] R. Alaei and M. Sheikhi, "Optical absorption of graphene nanoribbon in transverse and modulated longitudinal electric field," *Fullerenes, Nanotubes and Carbon Nanostructures*, vol. 21, no. 3, pp. 183–197, 2013.

[91] Y. Wei, W. Li, Y. Jiang, and J. Cheng, "Electric field induced injection and shift currents in zigzag graphene nanoribbons," *Physical Review B*, vol. 104, no. 11, p. 115402, 2021.

[92] Z. Zhang and W. Guo, "Energy-gap modulation of bn ribbons by transverse electric fields: First-principles calculations," *Physical Review B—Condensed Matter and Materials Physics*, vol. 77, no. 7, p. 075403, 2008.

[93] J. Majhi, S. K. Maiti, and S. Ganguly, "Enhanced current rectification in graphene nanoribbons: effects of geometries and orientations of nanopores," *Nanotechnology*, vol. 33, no. 25, p. 255704, 2022.

[94] E. C. Ahn, "2d materials for spintronic devices," *npj 2D Materials and Applications*, vol. 4, no. 1, p. 17, 2020.

[95] X. Li and J. Yang, "First-principles design of spintronics materials," *National Science Review*, vol. 3, no. 3, pp. 365–381, 2016.

[96] R. Meng, L. da Costa Pereira, J.-P. Locquet, V. Afanas' ev, G. Pourtois, and M. Houssa, "Hole-doping induced ferromagnetism in 2d materials," *npj Computational Materials*, vol. 8, no. 1, p. 230, 2022.

[97] R. Ma, N. V. Tepliakov, A. A. Mostofi, and M. Pizzochero, "Electrically tunable ultraflat bands and π-electron magnetism in graphene nanoribbons," *The Journal of Physical Chemistry Letters*, vol. 16, no. 7, pp. 1680–1685, 2025.

[98] Y. Chen, S. Xu, Y. Xie, C. Zhong, C. Wu, and S. Zhang, "Ferromagnetism and wigner crystallization in kagome graphene and related structures," *Physical Review B*, vol. 98, no. 3, p. 035135, 2018.

[99] Y.-W. Son, M. L. Cohen, and S. G. Louie, "Half-metallic graphene nanoribbons," *nature*, vol. 444, no. 7117, pp. 347–349, 2006.

[100] H. Xiang, B. Xu, Y. Xia, J. Yin, and Z. Liu, "Strain tunable magnetism in snx 2 (x= s, se) monolayers by hole doping," *Scientific reports*, vol. 6, no. 1, p. 39218, 2016.

[101] H. Chen, L. Yan, X.-l. Wang, J.-j. Xie, J. Lv, and H.-s. Wu, "Computational discovery of high-temperature ferromagnetic semiconductor monolayer h–mnn2," *ACS omega*, vol. 9, no. 1, pp. 1389–1397, 2023.

Appendix A

Supplementary Materials

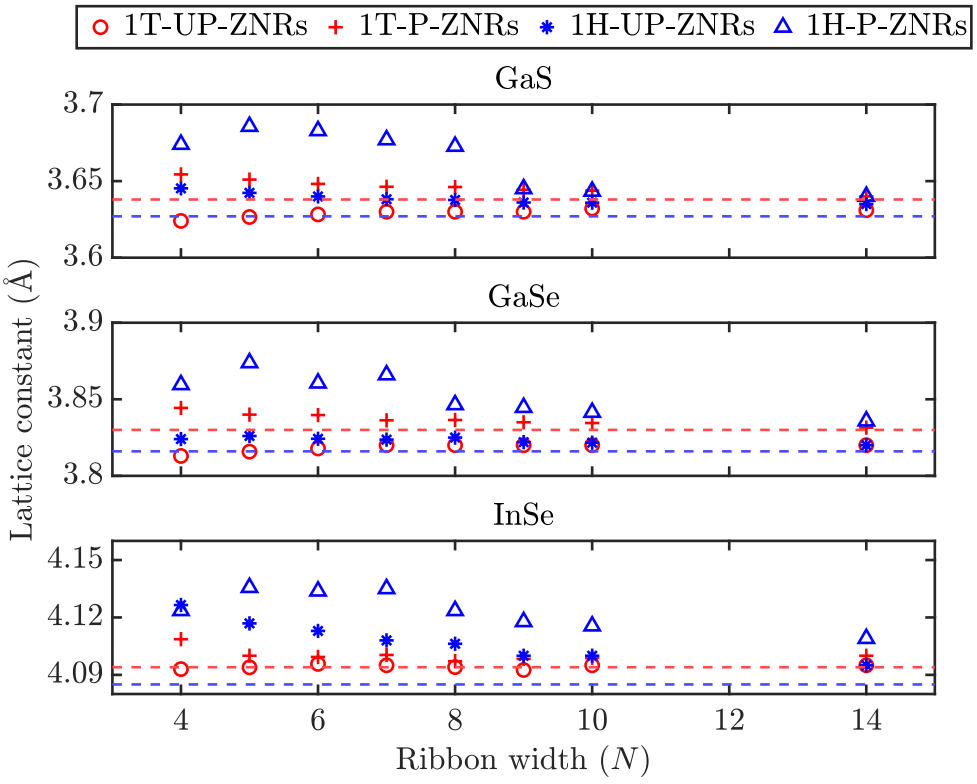

Figure A.1: Variation of the calculated lattice constants of MX ZNRs with ribbon width. Red and blue dashed lines show the calculated lattice constants of 2D 1T and 1H MXs, respectively. Adapted from Aliyev et al. [1] under a CC BY license.

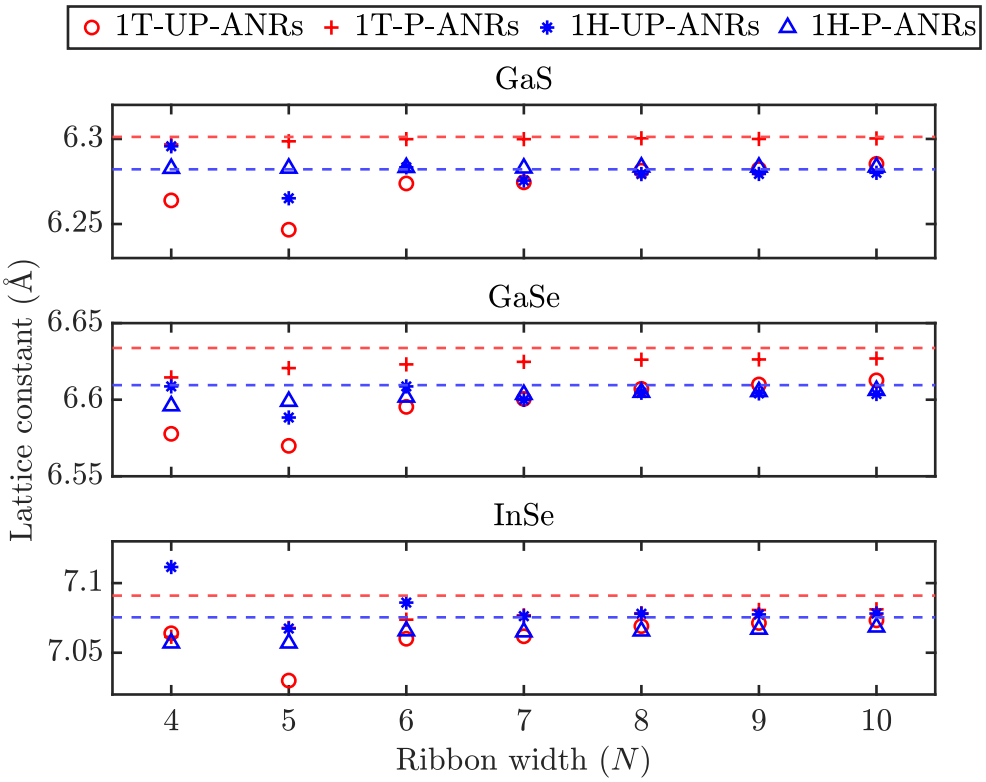

Figure A.2: Variation of the calculated lattice constants of MX ANRs with ribbon width. Red and blue dashed lines show the calculated lattice constants of 2D 1T and 1H MXs, respectively.

Table A.1: The calculated energy differences (ΔE) between 1T and 1H phase of 2D MXs and lattice constants of the structures are compared with previous works.

Material	This Work			Previous Work			Ref
	ΔE (meV)	1H Lattice Constant (Å)	1T Lattice Constant (Å)	ΔE (meV)	1H Lattice Constant (Å)	1T Lattice Constant (Å)	
GaS	20	3.63	3.64	20	3.63	3.64	[31]
GaSe	15	3.82	3.83	15	3.82	3.83	[31]
InSe	13	4.0	4.09	13	4.09	4.09	[78]

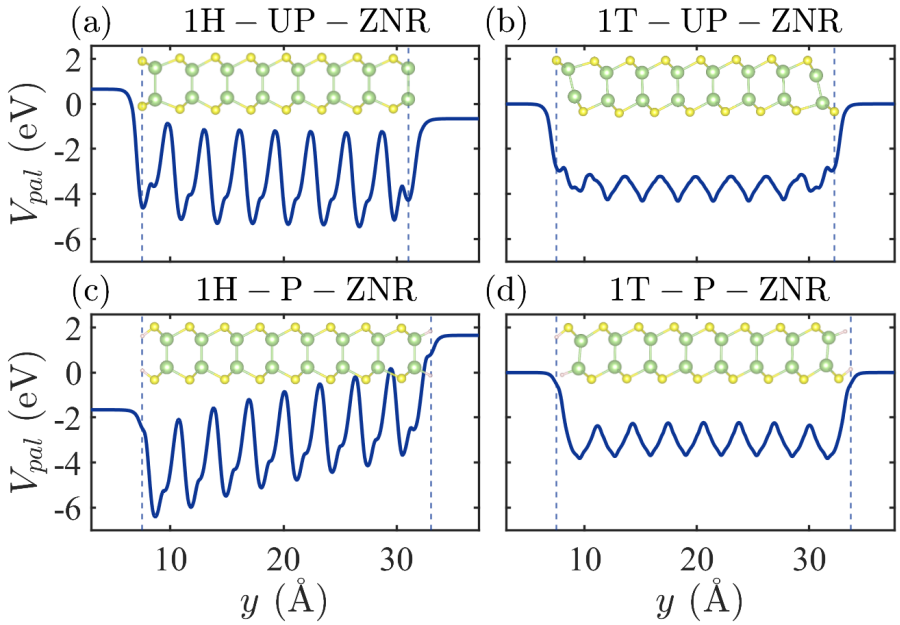

Figure A.3: Planar average of the local electrostatic potential of (a) UP-1H, (b) UP-1T, (c) P-1H, and (d) P-1T $N = 8$ GaS ZNRs. Reproduced from Aliyev et al. [1] under a CC BY license.

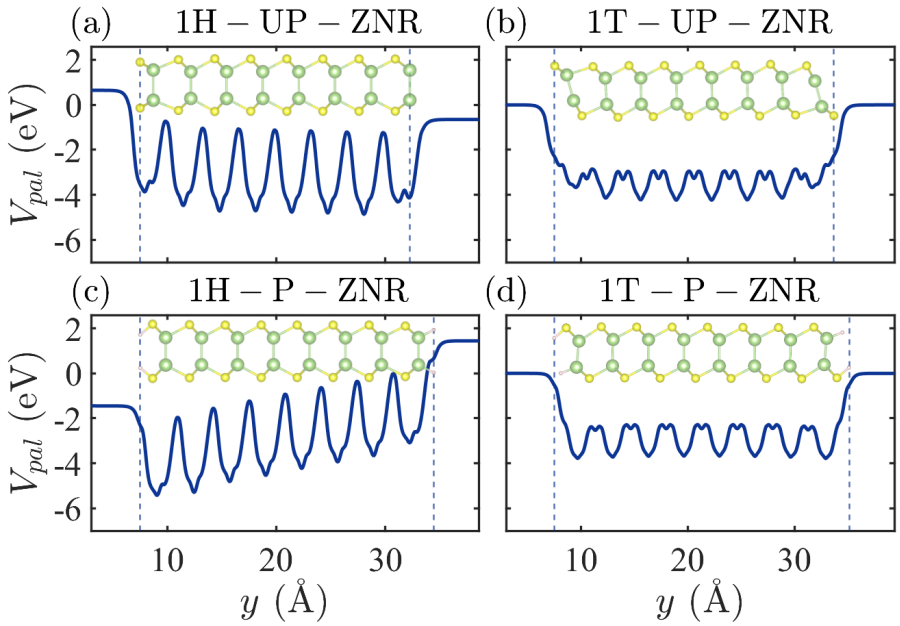

Figure A.4: Planar average of the local electrostatic potential of (a) UP-1H, (b) UP-1T, (c) P-1H, and (d) P-1T $N = 8$ GaSe ZNRs. Reproduced from Aliyev et al. [1] under a CC BY license.

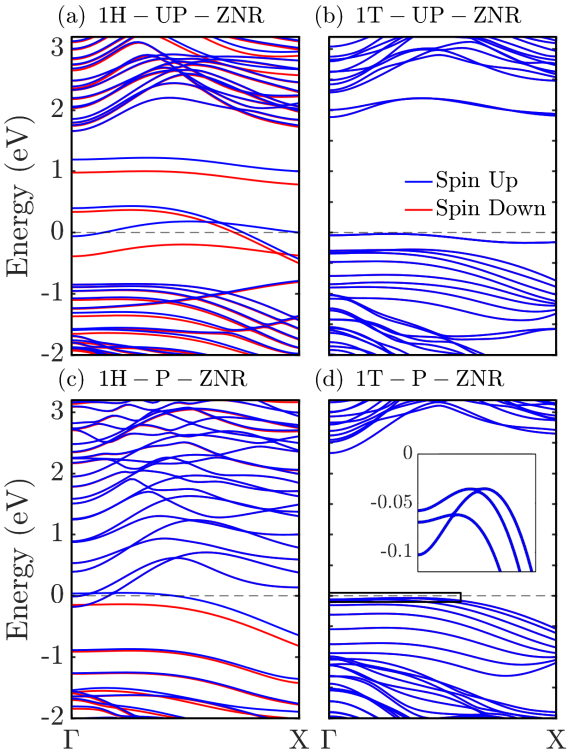

Figure A.5: Spin-polarized band structures of (a) unpassivated 1H, (b) unpassivated 1T, (c) passivated 1H and (d) passivated 1T $N = 8$ GaS ZNRs. Reproduced from Aliyev et al. [1] under a CC BY license.

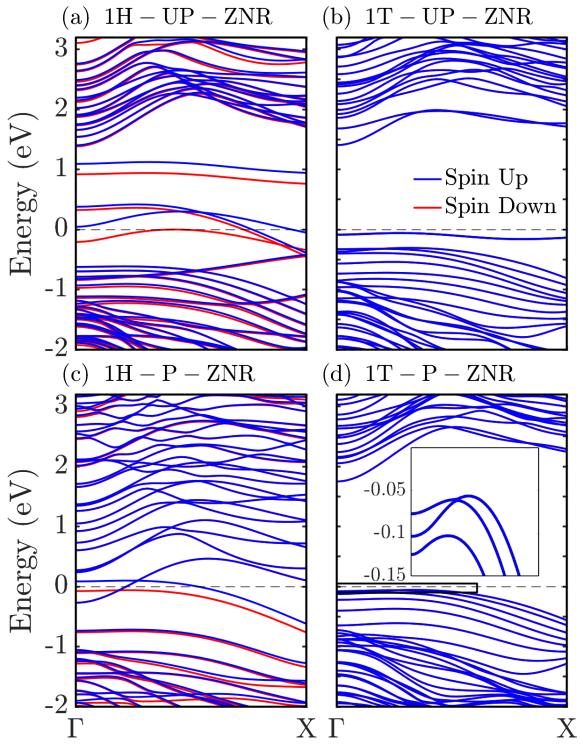

Figure A.6: Spin-polarized band structures of (a) unpassivated 1H, (b) unpassivated 1T, (c) passivated 1H and (d) passivated 1T $N = 8$ GaSe ZNRs. Reproduced from Aliyev et al. [1] under a CC BY license.

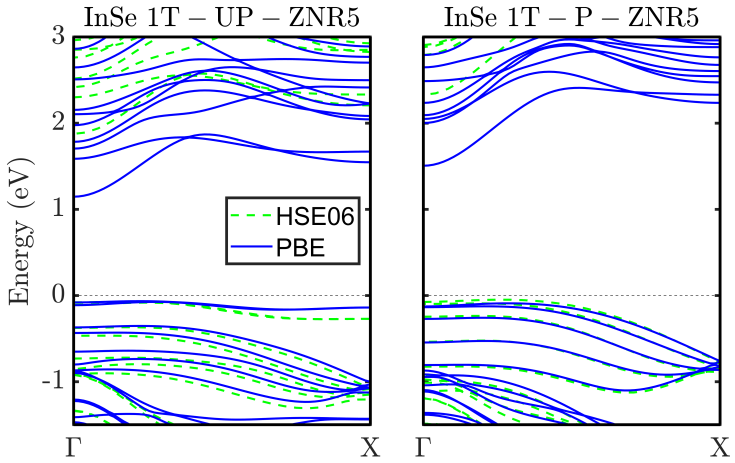

Figure A.7: Comparison of electronic band structures of InSe 1T-UP-ZNR and 1T-P-ZNR for $N = 5$, calculated using PBE and HSE06 functionals.

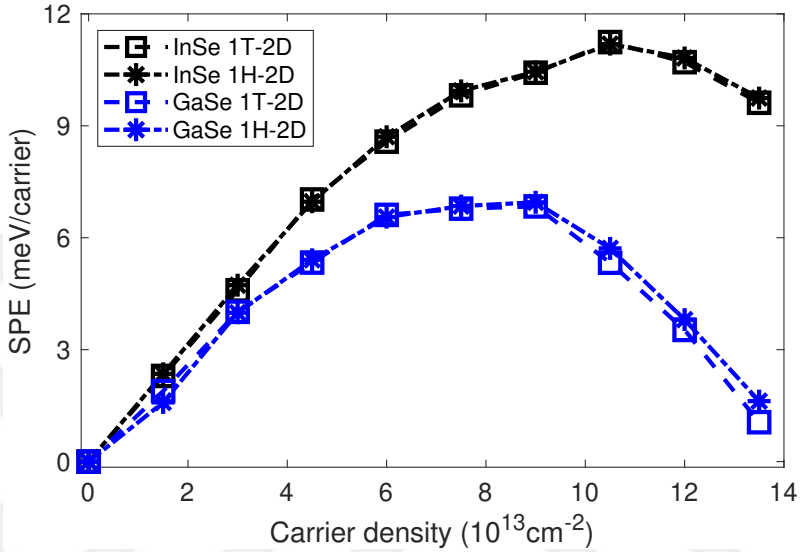

Figure A.8: 1H and 1T 2D InSe and GaSe spin polarization energies as a function of the carrier density.

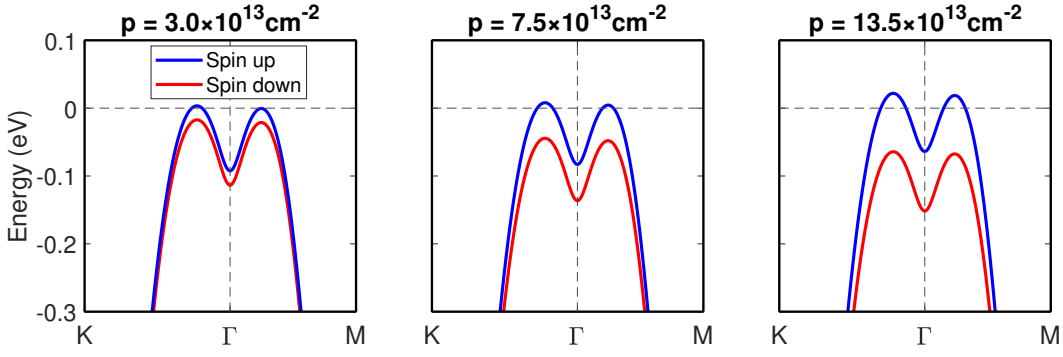

Figure A.9: Spin-polarized band structures of 2D 1T GaSe at different carrier densities.

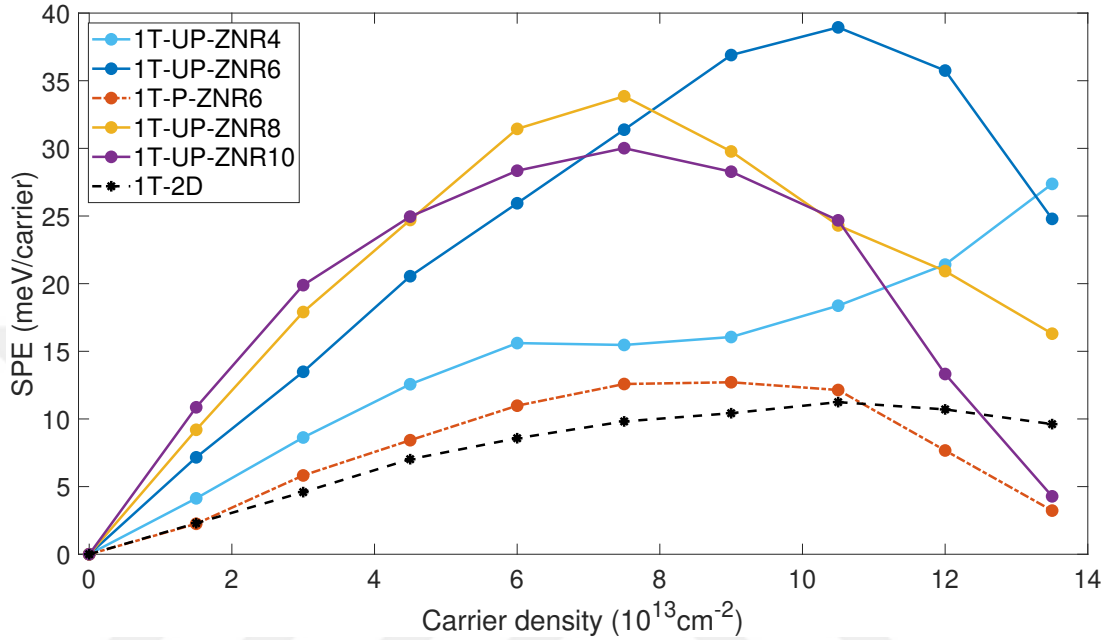

Figure A.10: Spin polarization energies as a function of the carrier density of all investigated InSe ZNRs.

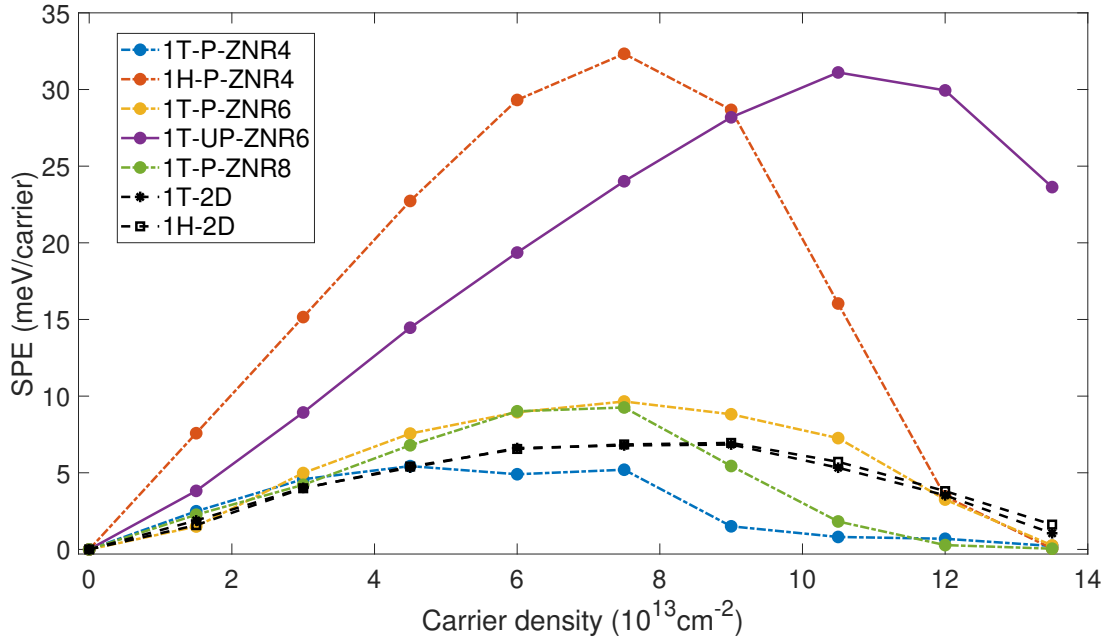

Figure A.11: Spin polarization energies as a function of the carrier density of all investigated InSe ZNRs.

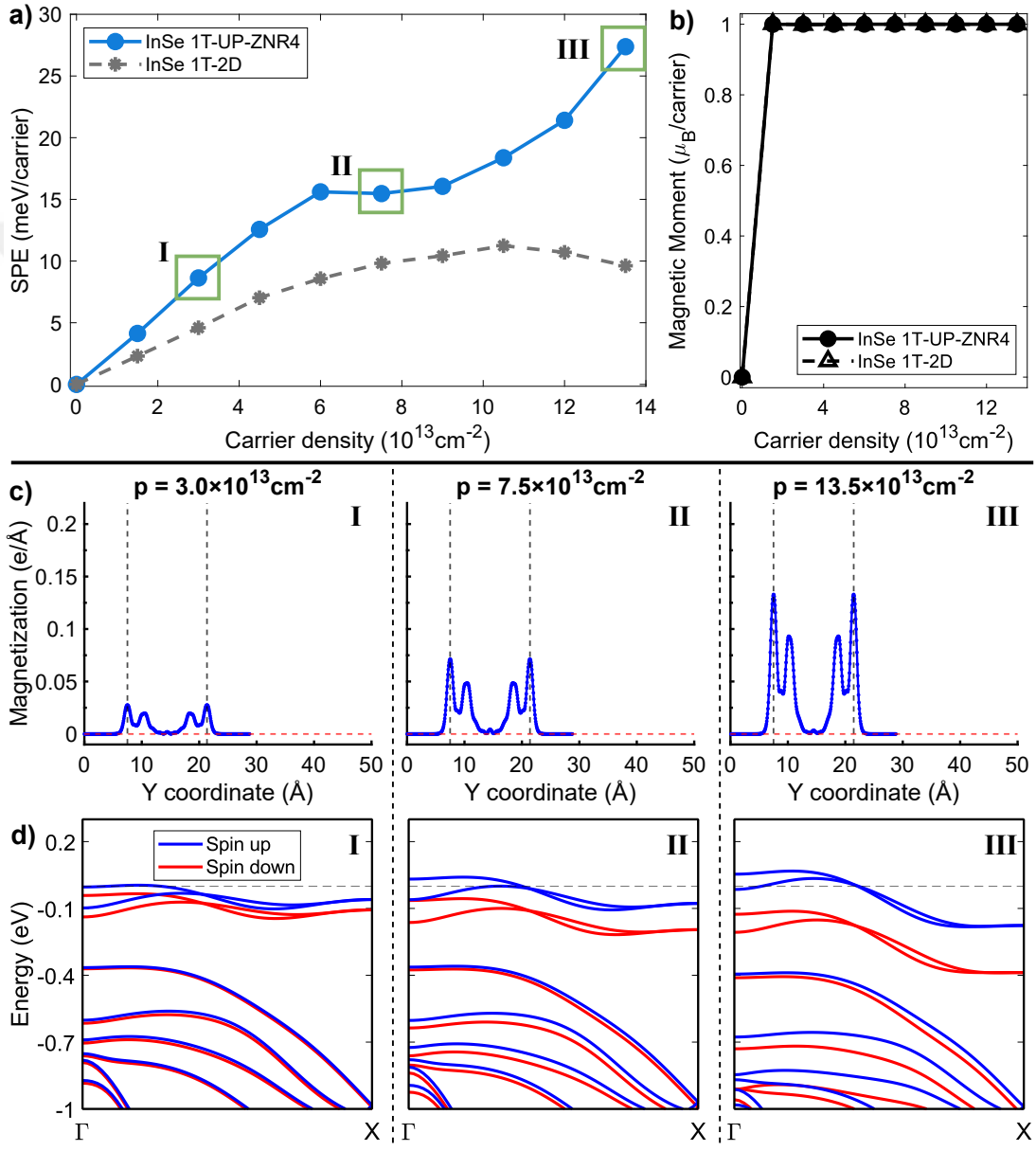

Figure A.12: InSe 1T-UP-ZNR4 and 1T-2D a) spin polarization energies and b) magnetic moments per carrier as a function of the carrier density. InSe 1T-UP-ZNR4 c) magnetization profiles along the width of NR and d) spin-polarized band structures at different carrier densities.

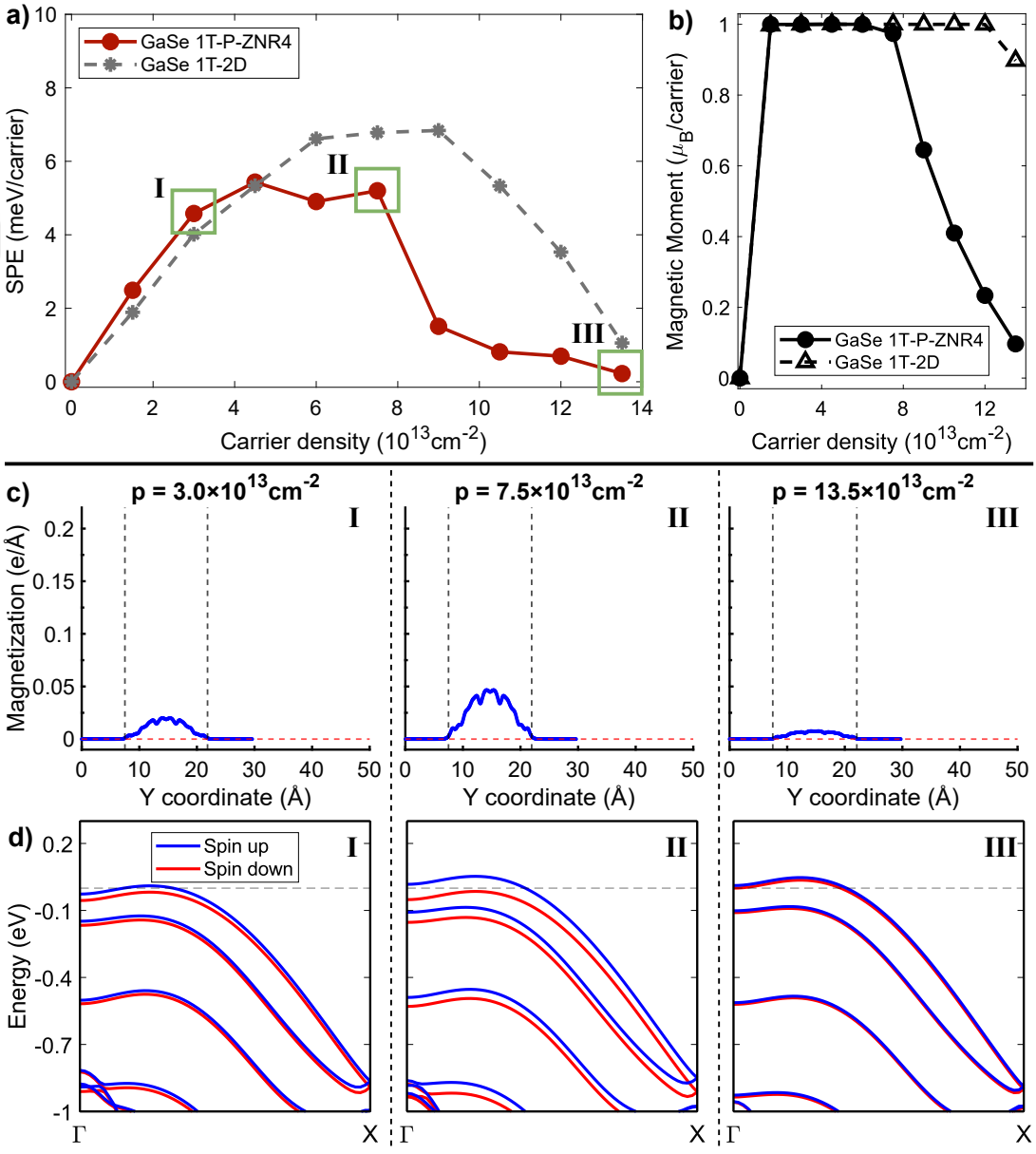

Figure A.13: GaSe 1T-P-ZNR4 and 1T-2D a) spin polarization energies and b) magnetic moments per carrier as a function of the carrier density. GaSe 1T-P-ZNR4 c) magnetization profiles along the width of NR and d) spin-polarized band structures at different carrier densities.

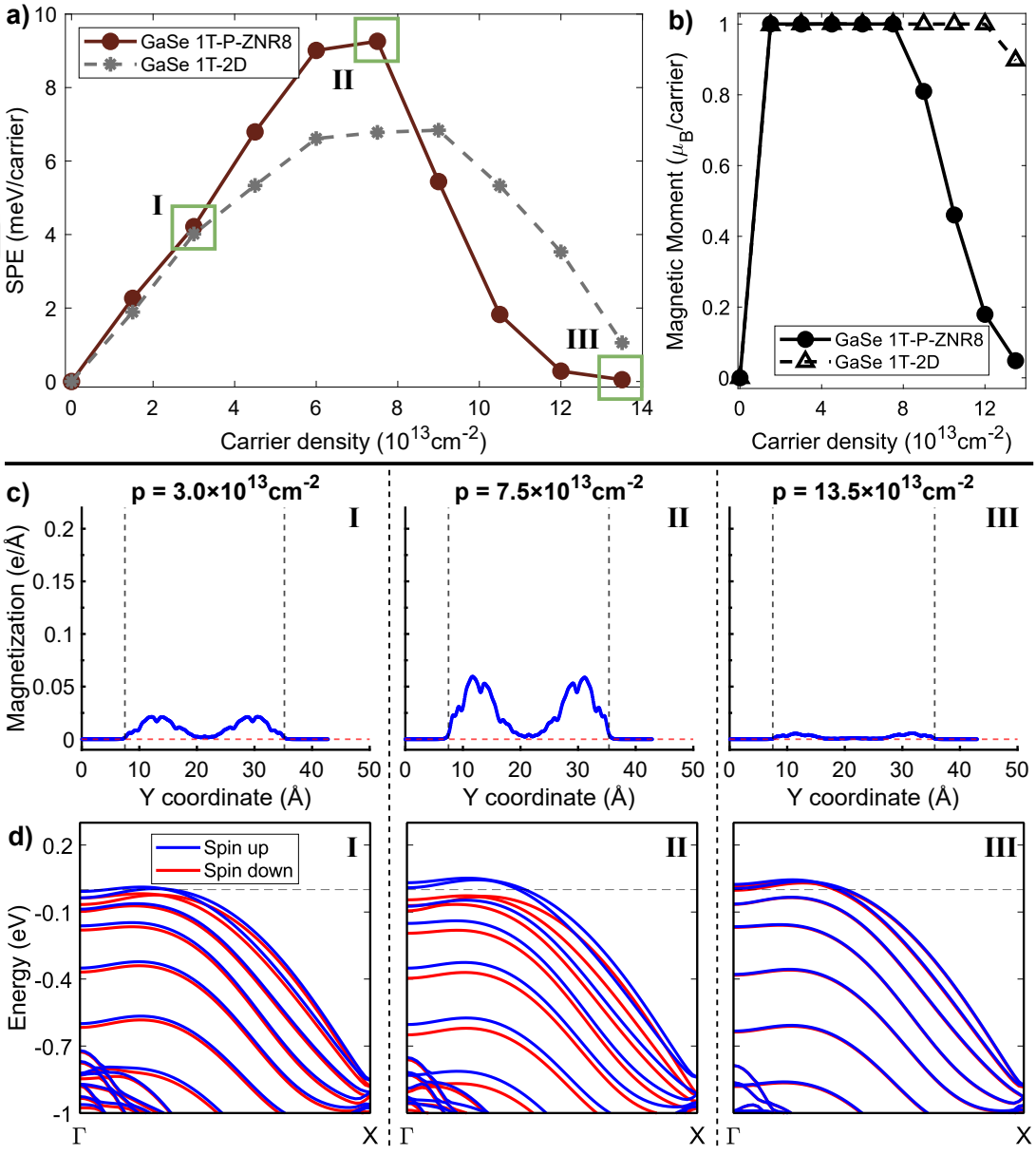

Figure A.14: GaSe 1T-P-ZNR8 and 1T-2D a) spin polarization energies and b) magnetic moments per carrier as a function of the carrier density. GaSe 1T-P-ZNR8 c) magnetization profiles along the width of NR and d) spin-polarized band structures at different carrier densities.

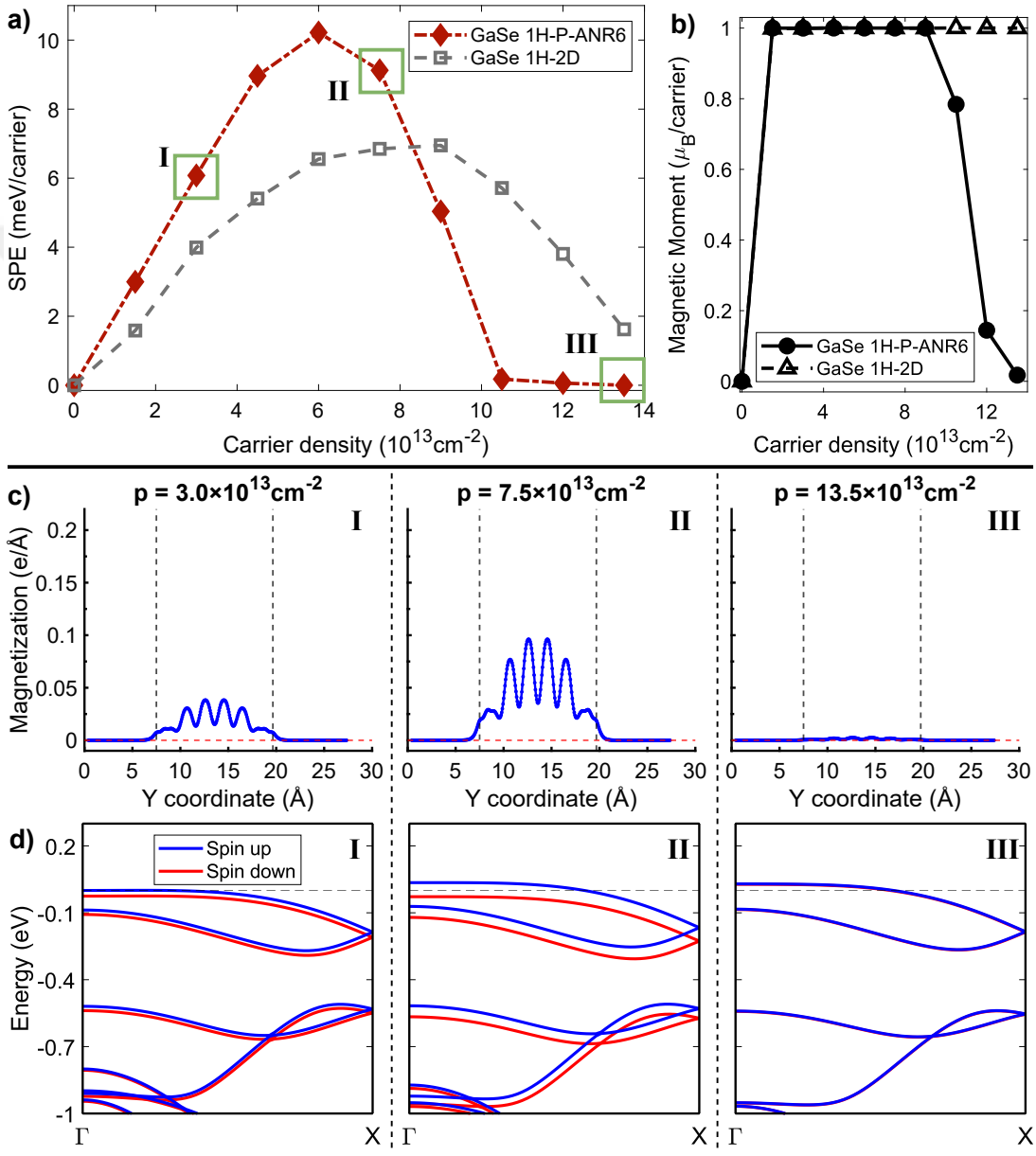

Figure A.15: GaSe 1H-P-ANR6 and 1H-2D a) spin polarization energies and b) magnetic moments per carrier as a function of the carrier density. GaSe 1H-P-ANR6 c) magnetization profiles along the width of NR and d) spin-polarized band structures at different carrier densities.

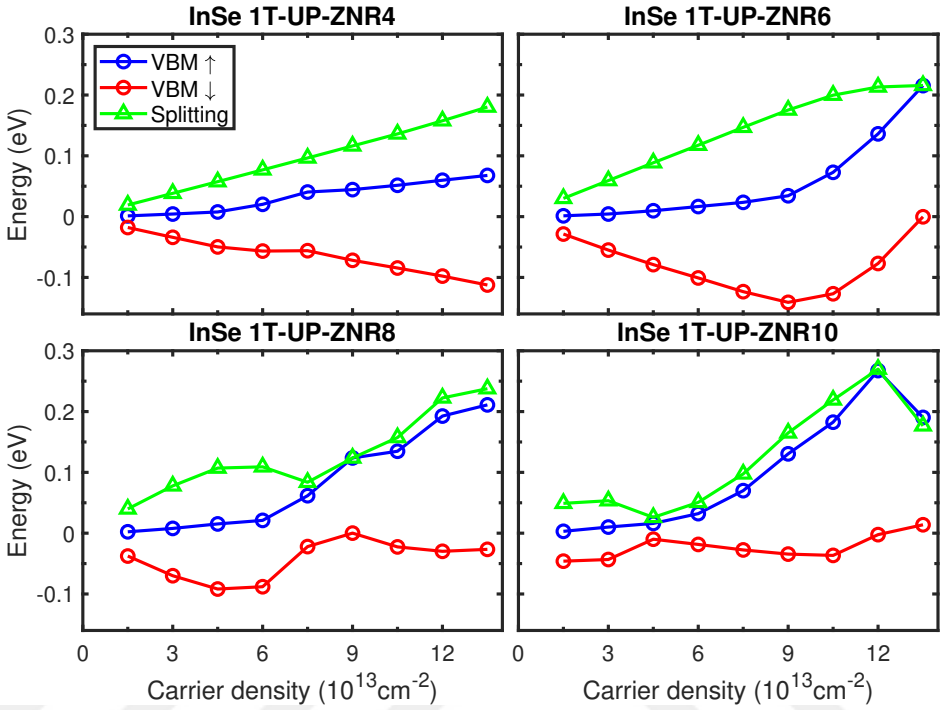

Figure A.16: InSe ZNRs VBM and spin splitting of the topmost valence band vs. carrier density.

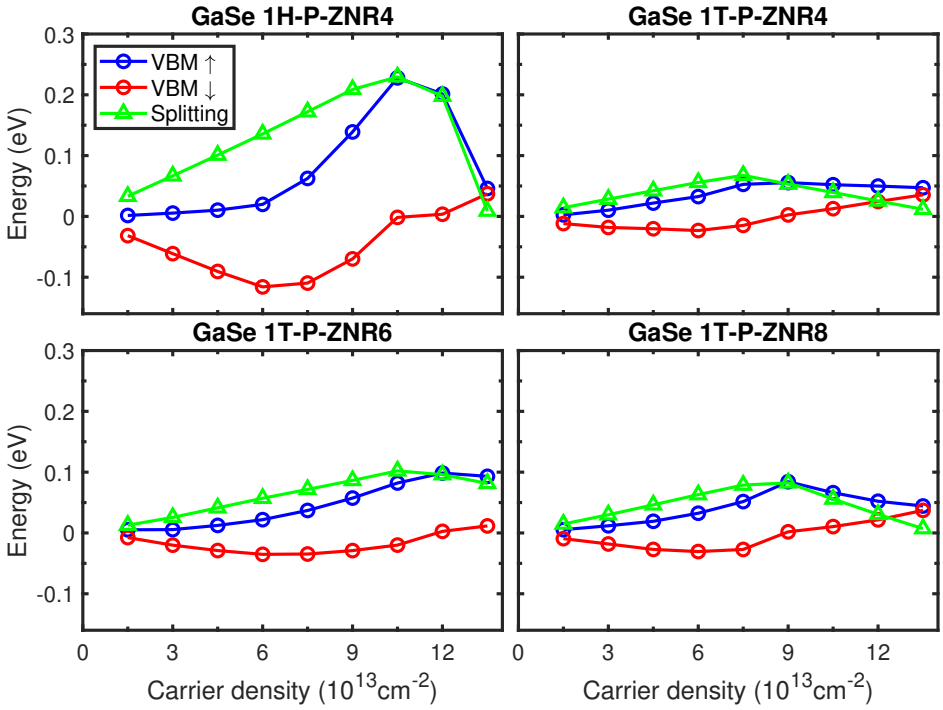

Figure A.17: GaSe ZNRs VBM and spin splitting of the topmost valence band vs. carrier density.